University of Basel

Markovian Master Equation for Continuous Charge Detection

Master Thesis

Qiuhan Wang

February 2026

Abstract

We develop a microscopic Markovian description of measurement-induced decoherence in semiconductor charge qubits monitored by a biased quantum-dot detector. Motivated by recent experiments showing detector-current–dependent decoherence, we model the double quantum dot (DQD) and the detector within a unified transport framework, where the detector tunneling rates depend on the DQD charge configuration via capacitive couplings. As a baseline, we first study a capacitively coupled single-dot sensing module and derive a Lindblad master equation that reduces to a Pauli rate equation, capturing state-dependent detector transport through interaction-conditioned tunneling channels. We then consider a coherent DQD coupled to the detector, derive a Lindblad master equation (using a secular treatment in the presence of DQD coherences), and evaluate the steady-state detector current together with an effective dephasing measure. In the fast-detector regime, a time-scale separation leads to an effective two-state dynamics for the DQD, where coherent inter-dot tunneling gives rise to incoherent transitions with rates proportional to $|g|^2$ and suppressed by detector effective dephasing measure. Both the current and the dephasing exhibit threshold features associated with the opening of transport channels through the detector, and the dephasing does not necessarily peak at the bias points of peaking charge sensitivity. This delineates operating regimes in which continuous readout remains informative while measurement backaction is relatively weak.

Supervised by:
Prof. Dr. Patrick Potts
Prof. Dr. Christoph Bruder

University of Basel
Quantum Thermodynamics Group
Switzerland

Disclaimer

In the course of composing this thesis, we utilized AI tools (primarily ChatGPT and DeepL Write) in a limited and supportive manner. Their use was mainly confined to refining sentence structure, improving clarity of expression, and enhancing overall readability. In addition, AI tools were occasionally used to assist with technical tasks such as identifying potential coding errors, suggesting debugging strategies, and improving code documentation or formatting.

It is important to emphasize that the core ideas, modeling choices, derivations, numerical implementation decisions, research findings, and analytical insights contained within this work are the result of our own efforts. The use of AI was strictly limited to aiding the articulation and presentation of these contributions and to streamlining routine technical troubleshooting; it did not generate the underlying scientific content nor replace independent reasoning.

Table of Contents

List of Symbols

Symbol	Description
ϵ_j	Single-particle on-site energy of dot $j \in \{D, S, L, R\}$.
U	Capacitive interaction energy between detector and target dot (SQD model).
U_L, U_R	Capacitive interaction energies between detector and left/right DQD sites (DQD model).
g	Coherent inter-dot tunneling amplitude (hybridization) in a double dot.
α	Reservoir/lead index.
μ	Chemical potential of a reservoir.
T	Temperature of a reservoir.
V	Bias voltage (chemical potential difference between two leads).
$n_F^\alpha(\omega)$	Fermi–Dirac distribution function of reservoir α.
κ_α	Tunneling rate between system and reservoir α (wide-band limit).
Γ	Total tunneling rate (sum of relevant tunneling rates).
I	Charge current.
$\langle\cdot\rangle$	Expectation value, $\langle\hat{O}\rangle = \mathrm{Tr}\{\hat{O}\hat{\rho}\}$.
$\langle\cdot\rangle_{ss}$	Steady-state expectation value.
$\mathrm{Tr}\{\cdot\}$	Trace over the system Hilbert space.
$\{\cdot,\cdot\}$	Anticommutator.
$\dagger$	Hermitian conjugate.
e	Elementary charge.

Fermionic Operator Relations

$\{\hat{d}, \hat{d}^\dagger\} = 1,$
$\{\hat{d}, \hat{d}\} = 0,$
$\{\hat{d}^\dagger, \hat{d}^\dagger\} = 0,$
$\hat{n} = \hat{d}^\dagger\hat{d},$
$\hat{n}^2 = \hat{n},$
$\hat{d}^2 = (\hat{d}^\dagger)^2 = 0.$

1 Introduction

Quantum bits (qubits) constitute the fundamental units of quantum information processing, providing a physical realization of a controllable two-level quantum system that can exist in coherent superpositions of its basis states. Over the past decades, a variety of solid-state platforms have been developed to implement qubits, including superconducting circuits [1], spin qubits in semiconductor quantum dots [2, 3], and charge qubits [4, 5]. These systems offer complementary advantages in terms of coherence times, controllability, scalability, and integration with existing fabrication technologies.

Among solid-state qubit platforms, charge qubits realized in semiconductor double quantum dots provide a conceptually simple and experimentally accessible implementation. In such systems, a single excess electron is confined to a pair of tunnel-coupled quantum dots, and the charge configurations $|1,0\rangle$ and $|0,1\rangle$, corresponding to the electron occupying the left or right dot, forming an effective two-level system. Coherent tunneling between the dots hybridizes these charge states, giving rise to delocalized eigenstates whose energy splitting is controlled by the interdot tunnel coupling and the electrostatic detuning. The resulting dynamics can be described by a minimal two-level Hamiltonian, where the detuning acts as a longitudinal field and the tunnel coupling induces coherent transitions between the charge states. Owing to their strong coupling to electric fields, charge qubits can be efficiently controlled and read out using purely electrical means, making them an attractive platform for studying quantum coherence and measurement in mesoscopic systems.

The same strong coupling to electric fields that enables efficient control and readout of charge qubits also makes them particularly sensitive to environmental fluctuations. In contrast to spin-based qubits, where decoherence is often dominated by magnetic noise, charge qubits primarily suffer from charge noise originating from nearby electrodes, background impurities, and dynamical charge rearrangements in the device environment. Fluctuations in the electrostatic potential directly translate into variations of the energy detuning between the charge states, leading to dephasing and limiting the coherence time. As a result, charge qubits typically exhibit shorter coherence times compared to other solid-state qubit platforms, despite their favorable controllability. Understanding the microscopic origins of these noise sources and their impact on qubit coherence is therefore essential for both improving device performance and elucidating the fundamental mechanisms of decoherence in electrically sensitive quantum systems.

Beyond uncontrolled environmental noise, an additional and conceptually distinct source of decoherence arises from the measurement process itself. In solid-state charge qubit experiments, the charge state is commonly monitored using nearby charge detectors, such as quantum point contacts [6, 7] or single-electron transistors [8, 9], which are capacitively coupled to the qubit. While such detectors enable high-fidelity, time-resolved readout, they are not passive elements: the detector constitutes an open quantum system with its own internal dynamics and fluctuations. Through capacitive coupling, charge fluctuations in the detector induce temporal variations of the qubit energy levels, giving rise to measurement backaction. This backaction can manifest as dephasing, relaxation, or excitation of the charge qubit, thereby directly affecting its coherence properties. Understanding how continuous charge detection influences qubit coherence is therefore crucial for interpreting experimental measurements and for assessing the fundamental limits imposed by quantum measurement in electrically sensitive qubit platforms.

Recent experimental progress has provided direct access to the coherence of charge qubits under continuous charge detection. In particular, experiments on double quantum dots capacitively coupled to a nearby quantum dot detector have enabled the controlled investigation of detector-induced backaction on an electronic two-level system [10]. By monitoring the qubit coherence using microwave spectroscopy while tuning the operating point and current of the charge detector, these studies have demonstrated that the decoherence rate of the charge qubit increases approximately linearly with the electric current through the charge detector. This observation provides clear evidence that continuous charge sensing constitutes a significant and tunable source of decoherence. Furthermore, a microscopic theory based on detector-induced detuning fluctuations captures the qualitative trends observed in the experiment, but quantitatively underestimates the measured decoherence rate. This discrepancy indicates that a complete theoretical understanding of measurement-induced decoherence in charge qubits remains an open challenge.

Motivated by this open discrepancy, in this work, we revisit the theoretical description of detector-induced decoherence in charge qubits from a modeling perspective. Rather than treating detector backaction as an effective noise source acting on the double quantum dots system, we explicitly consider the combined system of the double quantum dots and the charge detector within a unified Markovian framework. In contrast to previous theoretical descriptions [10], where the detector dynamics are assumed to be unaffected by the charge configuration of the double quantum dots and the detector current is treated as independent of it, our model accounts for the dependence of the detector current on the double quantum dots' charge state (see Supplemental Material therein). This allows us to capture the mutual backaction between the double quantum dots system and the detector and to distinguish more clearly between detector-induced charge fluctuations and decoherence associated with state-dependent charge detection. We first analyze the case of a single quantum dot subject to continuous charge detection, where the detector-induced dynamics can be characterized in a controlled and fully classical manner. Building on this foundation, we then extend the framework to a double quantum dot, which constitutes a genuine charge qubit, and investigate how detector backaction affects its coherence. By clarifying the assumptions underlying the effective description of measurement backaction, our work aims to provide a more transparent theoretical framework for interpreting recent experiments and for assessing the role of continuous charge sensing in electrically sensitive qubit platforms.

2 Single Quantum Dot: Classical model simulation

2.1 Overview and scope

This chapter establishes a detailed Markovian description of a capacitively coupled single-dot sensing setup, which will serve as the baseline building block for the DQD–detector analysis in Chapter 3. The system consists of a detector quantum dot biased by two electronic reservoirs (D_L and D_R) and a target quantum dot S coupled to a third reservoir B, with the two dots interacting only through an ideal capacitive coupling $U\hat{n}_D\hat{n}_S$ (Fig. 2.1). The capacitor forbids particle exchange between the dots while allowing electrostatic interaction, such that the occupation of one dot conditionally shifts the level of the other. In particular, the detector level is shifted from ϵ_D to $\epsilon_D + U$ depending on whether the target dot is empty or occupied. This conditional energy shift is the minimal mechanism by which the detector current becomes sensitive to the charge state of the target dot.

The primary goal of this chapter is not to develop open-system theory in general, but to provide a transparent and reproducible dynamical model for the detector–target module under non-equilibrium bias, including: (i) a master equation for the dot occupations under Born–Markov and weak-coupling assumptions, (ii) a consistent procedure to obtain the steady state and time-dependent populations, and (iii) explicit expressions for experimentally relevant observables such as stationary currents through the detector dot and their dependence on bias, temperature, and capacitive coupling. Because the Hamiltonian of the single quantum dot (SQD) module contains no coherent tunnelling between distinct charge configurations, the reduced density matrix remains diagonal in the occupation basis, and the dynamics reduce to a Pauli rate equation for the four charge states $\{|00\rangle, |01\rangle, |10\rangle, |11\rangle\}$. This simplification is not merely technical: it cleanly isolates the detector's transport-induced fluctuations and sets a controlled reference point before introducing coherence in the DQD system.

The outputs of this chapter will be used in two ways later. First, they provide a calibrated description of how detector transport depends on electrostatic shifts and reservoir parameters, which is essential for interpreting detector operation in the non-equilibrium regime. Second—and more importantly for the overall motivation of this thesis—the SQD module clarifies how a state-dependent current can emerge already at the level of classical charge configurations. Chapter 3 will build on this foundation by replacing the target dot with a coherent DQD system and by allowing the detector dynamics to depend on the DQD charge configuration, enabling a unified treatment of backaction beyond an effective-noise description.

2.2 Model and assumptions

The physical realization of the capacitively coupled setup is shown in Fig. 2.1. No particle exchange between the two dots is allowed; instead, they interact solely through an ideal capacitive coupling.

Following the structure established in the overview, the total Hamiltonian of the composite system and its fermionic environments is given by:

$$\hat{H}_{tot} = \hat{H}_S + \sum_{\alpha=D_L,D_R,B} \left(\hat{H}_\alpha + \hat{V}_\alpha\right) \tag{2.1}$$

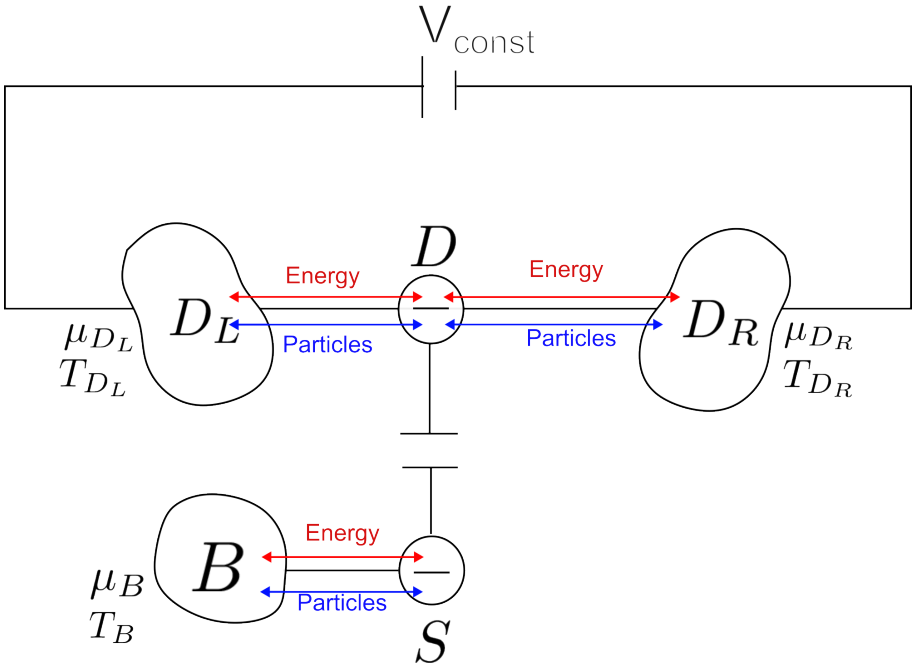

Figure 2.1: Schematic of the capacitively coupled single quantum dot (SQD) sensing setup. The detector dot (D) is tunnel-coupled to the left (D_L) and right (D_R) reservoirs, which are characterized by chemical potentials μ_{D_L}, μ_{D_R} and temperatures T_{D_L}, T_{D_R}, respectively. A bias voltage V_{const} drives a stationary particle current through the detector. The target dot (S) is coupled to an independent reservoir (B) with chemical potential μ_B and temperature T_B. The two dots are isolated from particle exchange and interact solely through an ideal capacitive coupling U, which induces a conditional shift in the energy levels depending on the mutual occupation $\hat{n}_D$ and $\hat{n}_S$.

where $\hat{H}_\alpha$ describes the non-interacting fermionic reservoirs and $\hat{V}_\alpha$ the tunnel coupling between each dot and its respective reservoir. The dot Hamiltonian reads

$$\hat{H}_S = \epsilon_D \hat{n}_D + \epsilon_S \hat{n}_S + U \hat{n}_D \cdot \hat{n}_S, \tag{2.2}$$

with $\hat{n}_j = \hat{d}_j^\dagger \hat{d}_j$ the occupation operator of dot j. The interaction term $U\hat{n}_D \cdot \hat{n}_S$ accounts for the electrostatic coupling mediated by the capacitor and leads to a conditional energy shift: the detector level is located at ϵ_D when the target dot is empty and at $\epsilon_D + U$ when it is occupied.

Each reservoir α is modeled as an equilibrium fermionic bath characterized by a chemical potential μ_α and temperature T_α,

$$\hat{H}_\alpha = \sum_q \epsilon_\alpha \hat{c}_{\alpha,q}^\dagger \hat{c}_{\alpha,q}, \tag{2.3}$$

and is coupled locally to its corresponding dot via standard tunneling Hamiltonians of the form

$$\hat{V}_\alpha = \sum_q \left(g_{\alpha,q} \hat{d}_\alpha \hat{c}_{\alpha,q}^\dagger - g_{\alpha,q}^* \hat{d}_\alpha^\dagger \hat{c}_{\alpha,q} \right). \tag{2.4}$$

Throughout this chapter, the reservoirs are assumed to remain in thermal equilibrium at all times, and their influence on the dot dynamics is fully characterized by Fermi–Dirac distributions $n_F^\alpha(\epsilon)$.

The reduced dynamics of the detector–target system is derived within the standard Born–Markov framework for open quantum systems. [11, 12] In this approach, the influence of the reservoirs on the dot dynamics is treated perturbatively.

We first introduce the *Born approximation*, which assumes weak coupling between the dot subsystem and the reservoirs. Under this condition, correlations between the system and the reservoirs remain negligible at all times, and the total density matrix can be approximated as

$$\hat{\rho}_{\mathrm{tot}}(t) \simeq \hat{\rho}(t) \otimes \hat{\rho}_{\mathrm{res}}, \tag{2.5}$$

where $\hat{\rho}(t)$ denotes the reduced density matrix of the dot subsystem and $\hat{\rho}_{\mathrm{res}}$ is the stationary equilibrium state of the reservoirs. Physically, this approximation requires the tunneling-induced energy scales to be small compared to the intrinsic energy scales of the dot system, such that higher-order tunneling processes can be neglected.

Next, the *Markov approximation* is applied. The reservoirs are assumed to exhibit rapidly decaying correlation functions, characterized by a correlation time

$$\tau_\alpha \sim \frac{\hbar}{k_B T_\alpha}, \tag{2.6}$$

which is much shorter than the characteristic timescale of the dot dynamics set by the tunneling rates. Throughout this thesis, we adopt natural units by setting $\hbar = 1$.

$$\tau_\alpha \ll \kappa_\alpha^{-1}. \tag{2.7}$$

This separation of timescales allows memory effects to be neglected and leads to a time-local master equation for the reduced density matrix.

The dot Hamiltonian contains no coherent tunneling between the detector and target dots. The two dots interact exclusively through a capacitive coupling term $U\hat{n}_D\hat{n}_S$, and the system–reservoir coupling operators act only on individual dot occupations. Consequently, the reduced density matrix remains diagonal in the charge occupation basis,

$$[\hat{n}_j, \hat{\rho}(t)] = 0. \tag{2.8}$$

This property implies that the dynamics of the SQD detector setup is purely incoherent and can be fully described in terms of occupation probabilities and transition rates.

Under these conditions, the Born–Markov approximation yields a master equation for the dot subsystem, which forms the basis for the transport and steady-state analysis presented in the following sections.

2.3 Markovian master equation

In this section we derive a Markovian master equation for the reduced density matrix of the dot subsystem (detector dot D and target dot S) within the Born–Markov framework introduced in Sec. 2.2. The derivation closely follows the standard interaction-picture treatment, specialized to fermionic reservoirs and to the capacitive coupling structure of the present model.

Based on the Hamiltonian in Sec. 2.2, we move to the interaction picture with respect to

$$\hat{H}_0 = \hat{H}_S + \sum_\alpha \hat{H}_\alpha, \tag{2.9}$$

so that operators transform as $\tilde{O}(t) = e^{+i\hat{H}_0 t}\hat{O}e^{-i\hat{H}_0 t}$ and the total density matrix $\tilde{\rho}_{\mathrm{tot}}(t)$ evolves

according to

$$\partial_t \tilde{\rho}_{\rm tot}(t) = -i[\tilde{V}(t), \tilde{\rho}_{\rm tot}(t)], \qquad \tilde{V}(t) = \sum_\alpha \tilde{V}_\alpha(t). \tag{2.10}$$

Under the Born approximation, $\tilde{\rho}_{\rm tot}(t) \simeq \tilde{\rho}(t) \otimes \hat{\rho}_{\rm res}$, with $\tilde{\rho}(t)$ the reduced density matrix of the dots and $\hat{\rho}_{\rm res} = \bigotimes_\alpha \hat{\rho}_\alpha$ the stationary reservoir state.

To apply the standard Born–Markov procedure, we write each coupling Hamiltonian in the form

$$\hat{V}_\alpha = \sum_k \hat{S}_{\alpha,k} \otimes \hat{B}_{\alpha,k}. \tag{2.11}$$

For fermionic tunneling couplings it is convenient to choose two system operators per reservoir:

$$\hat{S}_{\alpha,0} = \hat{d}_{\ell(\alpha)}, \qquad \hat{S}_{\alpha,1} = \hat{d}^\dagger_{\ell(\alpha)}, \tag{2.12}$$

where $\ell \in \{L, R\}$ labels the left and right detector reservoirs, then the corresponding bath operators

$$\hat{B}_{\alpha,0} = \sum_q g_{\alpha q} \hat{c}^\dagger_{\alpha q}, \qquad \hat{B}_{\alpha,1} = \sum_q g^*_{\alpha q} \hat{c}_{\alpha q}. \tag{2.13}$$

Denoting the reservoir correlation functions by

$$C^\alpha_{kk'}(s) = {\rm Tr}_\alpha \left[\tilde{B}^\dagger_{\alpha,k}(s) \tilde{B}_{\alpha,k'}(0) \tilde{\rho}_\alpha \right], \tag{2.14}$$

the standard Born–Markov equation in the interaction picture can be written as [11, 12]

$$\begin{aligned} \partial_t \tilde{\rho}(t) = \sum_\alpha \sum_{k,k'} \int_0^{+\infty} ds \, \Big\{ & C^\alpha_{kk'}(s) \left[\tilde{S}_{\alpha,k'}(t-s) \tilde{\rho}(t) \tilde{S}^\dagger_{\alpha,k}(t) - \tilde{S}^\dagger_{\alpha,k}(t) \tilde{S}_{\alpha,k'}(t-s) \tilde{\rho}(t) \right] \\ & + C^\alpha_{k'k}(-s) \left[\tilde{S}_{\alpha,k'}(t) \tilde{\rho}(t) \tilde{S}^\dagger_{\alpha,k}(t-s) - \tilde{\rho}(t) \tilde{S}^\dagger_{\alpha,k}(t-s) \tilde{S}_{\alpha,k'}(t) \right] \Big\}. \end{aligned} \tag{2.15}$$

Eq. (2.15) is the starting point for obtaining a time-local master equation for the dot subsystem.

The central model-specific ingredient is the interaction-picture form of the dot operators $\tilde{d}_D(t)$ and $\tilde{d}_S(t)$ under $\hat{H}_S$. Because $\hat{H}_S$ contains the interaction term $U\hat{n}_D\hat{n}_S$, the annihilation operators acquire different phases depending on the occupation of the other dot, leading to multiple Bohr frequencies.

For the detector-dot annihilation operator,

$$\tilde{S}_{D_L,0}(t) = e^{+i\hat{H}_S t} \hat{d}_D e^{-i\hat{H}_S t}, \tag{2.16}$$

one obtains (using the Baker–Campbell–Hausdorff expansion and the projector structure of $\hat{n}_S$), see Appendix A.

$$\tilde{d}_D(t) = e^{-i\epsilon_D t} \, \hat{d}_D(1 - \hat{n}_S) + e^{-i(\epsilon_D + U)t} \, \hat{d}_D \hat{n}_S. \tag{2.17}$$

Similarly,

$$\tilde{d}^\dagger_D(t) = e^{+i\epsilon_D t} \, \hat{d}^\dagger_D(1 - \hat{n}_S) + e^{+i(\epsilon_D + U)t} \, \hat{d}^\dagger_D \hat{n}_S. \tag{2.18}$$

For the target-dot operator $\hat{d}_S$ we obtain the analogous conditional evolution,

$$\tilde{d}_S(t) = e^{-i\epsilon_S t} \, \hat{d}_S(1 - \hat{n}_D) + e^{-i(\epsilon_S + U)t} \, \hat{d}_S \hat{n}_D, \tag{2.19}$$

and

$$\tilde{d}^\dagger_S(t) = e^{+i\epsilon_S t} \, \hat{d}^\dagger_S(1 - \hat{n}_D) + e^{+i(\epsilon_S + U)t} \, \hat{d}^\dagger_S \hat{n}_D. \tag{2.20}$$

Eqs. (2.17)–(2.20) show explicitly that each tunnel coupling contains two characteristic frequencies per dot: the bare level ϵ_j and the Coulomb-shifted level ϵ_j+U. This frequency splitting is the origin of the fast oscillating factors $e^{\pm iUt}$ that appear when different Bohr frequencies are coupled in the non-secular treatment.

To proceed, we write the interaction-picture system operators as sums of eigenoperators oscillating with definite Bohr frequencies,

$$\tilde{S}_{\alpha,k}(t) = \sum_j e^{-i\omega_j t}\, \hat{S}^{(j)}_{\alpha,k}, \tag{2.21}$$

where the set of frequencies is $\omega_j \in \{\epsilon_D, \epsilon_D+U\}$ for $\alpha \in \{D_L, D_R\}$ and $\omega_j \in \{\epsilon_S, \epsilon_S+U\}$ for $\alpha = B$. Inserting this decomposition into Eq. (2.15), one arrives at

$$\partial_t \tilde{\rho}(t) = \sum_\alpha \sum_{k,k'} \sum_{j,j'} e^{i(\omega_j-\omega_{j'})t}\, \Gamma^\alpha_{kk'}(\omega_j) \left[\tilde{S}^{(j')}_{\alpha,k'}\tilde{\rho}(t)\left(\tilde{S}^{(j)}_{\alpha,k}\right)^\dagger - \left(\tilde{S}^{(j)}_{\alpha,k}\right)^\dagger \tilde{S}^{(j')}_{\alpha,k'}\tilde{\rho}(t)\right] + \text{H.c.}, \tag{2.22}$$

with the one-sided Fourier transforms of reservoir correlations

$$\Gamma^\alpha_{kk'}(\omega) = \int_0^\infty ds\, e^{i\omega s} C^\alpha_{kk'}(s) = \frac{1}{2}\gamma^\alpha_{kk'}(\omega) + i\Delta^\alpha_{kk'}(\omega). \tag{2.23}$$

Here $\gamma^\alpha_{kk'}(\omega)$ are dissipative rates and $\Delta^\alpha_{kk'}(\omega)$ generate the Lamb-shift Hamiltonian.

For fermionic reservoirs in equilibrium, the cross-correlations vanish for $k \neq k'$, and the non-zero dissipative rates take the form [12]

$$\gamma^\alpha_{00}(\omega) = \kappa_\alpha\left[1 - n^\alpha_F(\omega)\right], \qquad \gamma^\alpha_{11}(\omega) = \kappa_\alpha n^\alpha_F(\omega), \tag{2.24}$$

where $n^\alpha_F(\epsilon) = \left[1 + e^{(\epsilon-\mu_\alpha)/(k_B T_\alpha)}\right]^{-1}$ is the Fermi function and κ_α is the (wide-band) tunneling rate. The dispersive contributions generate a Lamb-shift Hamiltonian $\hat{H}_{\text{LS}}$ in the Schrödinger picture. Since $\hat{H}_{\text{LS}}$ does not affect the transport observables considered in this thesis, we neglect it in the following.

If the secular approximation is performed under the condition $\kappa_\alpha \ll U$, only terms with $j = j'$ survive in Eq. (2.22). This simplification yields a master equation in the Gorini-Kossakowski-Sudarshan-Lindblad (GKLS) form:

$$\partial_t \tilde{\rho}(t) = \sum_{\alpha,k,j} \gamma^\alpha_k(\omega_j)\mathcal{D}[\tilde{S}^{(j)}_{\alpha,k}]\tilde{\rho}(t), \tag{2.25}$$

where the dissipator is defined as $\mathcal{D}[\hat{L}]\hat{\rho} \equiv \hat{L}\hat{\rho}\hat{L}^\dagger - \frac{1}{2}\{\hat{L}^\dagger\hat{L}, \hat{\rho}\}$. This structure, named after Gorini, Kossakowski, Sudarshan [13] and Lindblad [14], represents the most general linear, trace-preserving, and completely positive (CPTP) generator for the dynamics of an open quantum system.

Transforming back to the Schrödinger picture gives

$$\partial_t \hat{\rho}(t) = -i[\hat{H}_S, \hat{\rho}(t)] + \sum_{\alpha,k,j} \gamma^\alpha_k(\omega_j)\, \mathcal{D}\left[\hat{S}^{(j)}_{\alpha,k}\right]\hat{\rho}(t). \tag{2.26}$$

Without the secular approximation, Eq. (2.22) contains terms with $j \neq j'$ accompanied by oscillating factors $e^{\pm i(\omega_j-\omega_{j'})t}$. For the present SQD setup, however, the reduced density matrix remains diagonal in the charge-occupation basis (Eq. (2.8)) and no coherences between different charge states are generated. As a consequence, the non-secular cross terms do not contribute,

and the master equation reduces to a time-independent GKLS form without invoking the secular approximation. This simplification is specific to the incoherent SQD setup and does not apply to the coherent DQD case discussed in Chapter 3.

Using Eqs. (2.17)–(2.20) and the dissipative rates in Eq. (2.24), one obtains an explicit Schrödinger-picture GKLS equation of the form

$$\begin{aligned}\partial_t\hat{\rho}(t) = &-i[\hat{H}_S,\hat{\rho}(t)] \qquad (2.27)\\ &+\sum_{\alpha\in\{D_L,D_R\}}\Big[\kappa_\alpha\big(1-n_F^\alpha(\epsilon_D)\big)\,\mathcal{D}\Big[\hat{d}_D(1-\hat{n}_S)\Big]\,\hat{\rho}(t)+\kappa_\alpha n_F^\alpha(\epsilon_D)\,\mathcal{D}\Big[\hat{d}_D^\dagger(1-\hat{n}_S)\Big]\,\hat{\rho}(t)\\ &+\kappa_\alpha\big(1-n_F^\alpha(\epsilon_D+U)\big)\,\mathcal{D}\Big[\hat{d}_D\hat{n}_S\Big]\,\hat{\rho}(t)+\kappa_\alpha n_F^\alpha(\epsilon_D+U)\,\mathcal{D}\Big[\hat{d}_D^\dagger\hat{n}_S\Big]\,\hat{\rho}(t)\Big]\\ &+\kappa_B\big(1-n_F^B(\epsilon_S)\big)\,\mathcal{D}\Big[\hat{d}_S(1-\hat{n}_D)\Big]\,\hat{\rho}(t)+\kappa_B n_F^B(\epsilon_S)\,\mathcal{D}\Big[\hat{d}_S^\dagger(1-\hat{n}_D)\Big]\,\hat{\rho}(t)\\ &+\kappa_B\big(1-n_F^B(\epsilon_S+U)\big)\,\mathcal{D}\Big[\hat{d}_S\hat{n}_D\Big]\,\hat{\rho}(t)+\kappa_B n_F^B(\epsilon_S+U)\,\mathcal{D}\Big[\hat{d}_S^\dagger\hat{n}_D\Big]\,\hat{\rho}(t). \qquad (2.28)\end{aligned}$$

Eq. (2.28) is the central result of this section. It has a transparent interpretation in terms of conditional tunneling channels. The dissipators proportional to $\kappa_\alpha\big[1-n_F^\alpha(\cdot)\big]$ describe electron extraction from the detector dot into reservoir $\alpha\in\{D_L,D_R\}$, while the terms proportional to $\kappa_\alpha n_F^\alpha(\cdot)$ describe injection from reservoir α into the detector dot. The factors $(1-\hat{n}_S)$ and $\hat{n}_S$ act as projectors on the charge state of the target dot and select whether the detector level is at ϵ_D (for $\hat{n}_S=0$) or shifted to ϵ_D+U (for $\hat{n}_S=1$). Analogously, the last four dissipators describe tunneling between the target dot and its reservoir B. Here $(1-\hat{n}_D)$ and $\hat{n}_D$ project on the detector occupation and select whether the target level is at ϵ_S or shifted to ϵ_S+U.

Eq. (2.28) provides a complete Markovian description of the SQD detector module, where tunneling events through each reservoir occur through two interaction-conditioned transport channels, corresponding to energies ϵ_j and ϵ_j+U.

In the next section we use Eq. (2.28) to derive the rate equations for the charge-state populations, compute the stationary state, and evaluate the detector and target currents in the non-equilibrium regime.

2.4 Steady-state solution and transport currents

The Markovian master equation derived in Sec. 2.3 provides a complete description of the reduced dynamics of the SQD detector setup. In this section we exploit the structural properties of the model to obtain rate equations for the charge-state populations, determine the steady state, and evaluate the particle currents through the detector and target dots.

As discussed in Sec. 2.3, the absence of coherent tunneling between the dots and the purely capacitive interaction imply that the reduced density matrix remains diagonal in the charge occupation basis, see Eq. (2.8). Consequently, coherences between different charge sectors are neither generated nor sustained by the dynamics. The reduced density matrix can therefore be written as

$$\hat{\rho}(t)=p_{00}(t)\,|00\rangle\langle 00|+p_{01}(t)\,|01\rangle\langle 01|+p_{10}(t)\,|10\rangle\langle 10|+p_{11}(t)\,|11\rangle\langle 11|\,, \qquad (2.29)$$

where $|n_Dn_S\rangle$ denotes the state with occupation numbers $n_D,n_S\in\{0,1\}$ of the detector and target dots, respectively.

Inserting Eq. (2.29) into the GKLS master eq. (2.28), the dynamics reduces to a Pauli-type master equation for the populations $p_{ij}(t)$. Each dissipator contributes a transition between two charge configurations, with rates determined by the corresponding Fermi functions of the reservoirs.

Collecting all gain and loss terms, the population dynamics reads

$$\begin{aligned}
\dot{p}_{00} &= \alpha^{D_L}_{10\to00}p_{10} + \alpha^{D_R}_{10\to00}p_{10} + \alpha^{B}_{01\to00}p_{01} - \beta^{D_L}_{00\to10}p_{00} - \beta^{D_R}_{00\to10}p_{00} - \beta^{B}_{00\to01}p_{00},\\
\dot{p}_{01} &= \alpha^{D_L}_{11\to01}p_{11} + \alpha^{D_R}_{11\to01}p_{11} + \beta^{B}_{00\to01}p_{00} - \alpha^{B}_{01\to00}p_{01} - \beta^{D_L}_{01\to11}p_{01} - \beta^{D_R}_{01\to11}p_{01},\\
\dot{p}_{10} &= \alpha^{B}_{11\to10}p_{11} + \beta^{D_L}_{00\to10}p_{00} + \beta^{D_R}_{00\to10}p_{00} - \alpha^{D_L}_{10\to00}p_{10} - \alpha^{D_R}_{10\to00}p_{10} - \beta^{B}_{10\to11}p_{10},\\
\dot{p}_{11} &= \beta^{D_L}_{01\to11}p_{01} + \beta^{D_R}_{01\to11}p_{01} + \beta^{B}_{10\to11}p_{10} - \alpha^{D_L}_{11\to01}p_{11} - \alpha^{D_R}_{11\to01}p_{11} - \alpha^{B}_{11\to10}p_{11}.
\end{aligned} \tag{2.30}$$

Here $\alpha^{\alpha}_{i\to j}$ and $\beta^{\alpha}_{i\to j}$ denote particle extraction and injection rates associated with reservoir α.

The explicit expressions follow directly from the dissipative rates in Eq. (2.24):

$$\alpha^{D_\ell}_{10\to00} = \kappa_{D_\ell}\left[1 - n_F^{D_\ell}(\epsilon_D)\right], \qquad \beta^{D_\ell}_{00\to10} = \kappa_{D_\ell} n_F^{D_\ell}(\epsilon_D), \tag{2.31}$$

$$\alpha^{D_\ell}_{11\to01} = \kappa_{D_\ell}\left[1 - n_F^{D_\ell}(\epsilon_D + U)\right], \qquad \beta^{D_\ell}_{01\to11} = \kappa_{D_\ell} n_F^{D_\ell}(\epsilon_D + U), \tag{2.32}$$

$$\alpha^{B}_{01\to00} = \kappa_B\left[1 - n_F^{B}(\epsilon_S)\right], \qquad \beta^{B}_{00\to01} = \kappa_B n_F^{B}(\epsilon_S), \tag{2.33}$$

$$\alpha^{B}_{11\to10} = \kappa_B\left[1 - n_F^{B}(\epsilon_S + U)\right], \qquad \beta^{B}_{10\to11} = \kappa_B n_F^{B}(\epsilon_S + U). \tag{2.34}$$

The steady state $\bar{\rho}$ is defined by $\dot{p}_{ij} = 0$ together with the normalization condition

$$p_{00} + p_{01} + p_{10} + p_{11} = 1. \tag{2.35}$$

This yields a linear system of equations for the steady-state populations $\{\bar{p}_{ij}\}$, which can be solved analytically in limiting cases or numerically for general parameters.

The steady-state occupations encode the conditional dynamics of the detector: the occupation of the target dot S controls which transport channel of the detector dot D—at energy ϵ_D or $\epsilon_D + U$—is available, thereby modulating the detector current.

The particle current associated with a given reservoir is defined as the rate of change of its electron number. For the left detector reservoir D_L, the current is formally defined as:

$$I_{D_L} \equiv -e\frac{d}{dt}\langle \hat{N}_{D_L}\rangle, \qquad \hat{N}_{D_L} = \sum_q \hat{c}^\dagger_{D_L,q}\hat{c}_{D_L,q}. \tag{2.36}$$

With this convention, $I_{D_L} > 0$ corresponds to a net flow of electrons *from* the reservoir D_L *into* the detector dot. In the steady state, charge conservation strictly implies $I_{D_L} = -I_{D_R}$.Within the Markovian master equation framework, transport is fully encoded in the dissipative terms. The current can be evaluated directly from the reduced density matrix by taking the trace over the associated quantum jump superoperators, $\mathcal{J}[\hat{O}]\rho \equiv \hat{O}\rho\hat{O}^\dagger$. Since electron tunneling *into* the detector corresponds to $\hat{d}^\dagger_D$-type jumps and tunneling *out of* the detector corresponds to $\hat{d}_D$-type jumps, the steady-state current from D_L evaluates to

$$I_{D_L} = -e\mathrm{Tr}\left[\sum_{n_S=0,1}\left(\Gamma^1_{D_L,n_S}\mathcal{J}[\hat{d}^\dagger_D\hat{P}_{n_S}] - \Gamma^0_{D_L,n_S}\mathcal{J}[\hat{d}_D\hat{P}_{n_S}]\right)\bar{\rho}\right], \tag{2.37}$$

where $\hat{P}_{n_S} = |n_S\rangle\langle n_S|$ projects onto the target dot charge state, and the state-dependent tunneling rates $\Gamma^{0/1}$ are given by the injection/extraction coefficients defined in Eqs. (2.31)-(2.34). This abstract trace becomes physically transparent when evaluated in the occupation basis $|n_D, n_S\rangle$. Because the jump operators strictly toggle the detector occupation between 0 and 1, the trace reduces to a classical balance equation depending only on the joint populations $\bar{p}_{n_D,n_S}$. Using

the explicit rate definitions, we recover the intuitive result:

$$I_{D_L} = -e\left[\beta^{D_L}_{00\to10}\bar{p}_{00} + \beta^{D_L}_{01\to11}\bar{p}_{01} - \alpha^{D_L}_{10\to00}\bar{p}_{10} - \alpha^{D_L}_{11\to01}\bar{p}_{11}\right]. \tag{2.38}$$

Similarly, the current associated with the target-dot reservoir B reads

$$I_B = -e\Big[\beta^{B}_{00\to01}\bar{p}_{00} + \beta^{B}_{10\to11}\bar{p}_{10} - \alpha^{B}_{01\to00}\bar{p}_{01} - \alpha^{B}_{11\to10}\bar{p}_{11}\Big]. \tag{2.39}$$

These expressions make explicit that transport through each reservoir is governed by a balance between particle injection and extraction processes, weighted by the corresponding steady-state occupation probabilities. In particular, the detector current depends sensitively on the occupation of the target dot, illustrating how charge sensing emerges naturally from the capacitive coupling between the two dots.

Throughout this work, energies are expressed in units of the interaction strength U. Temperatures are given explicitly in units of k_BT/U. This includes the dot energies ϵ_D, ϵ_S, the interaction strength U, the chemical potentials μ_α, and the applied bias voltage

$$V = \mu_{D_L} - \mu_{D_R}. \tag{2.40}$$

The tunneling rates κ_{D_L}, κ_{D_R}, and κ_B are expressed in the same units.

We define the total detector tunneling rate

$$\Gamma = \kappa_{D_L} + \kappa_{D_R}, \tag{2.41}$$

which sets the characteristic timescale for charge transfer through the detector dot. All currents are presented in dimensionless form as $I/(e\Gamma)$.

In the following section, we analyze the steady-state currents as functions of the bias voltage, source chemical potential, and temperature, and discuss the resulting transport regimes and phase diagrams.

2.5 Steady-state transport characteristics

In this section, we analyze the steady-state transport properties obtained from the rate equations derived in Sec. 2.4. We focus on the detector current and its dependence on the applied bias voltage, the source chemical potential, and temperature, and discuss the physical mechanisms underlying the observed features.

Figure 2.2 summarizes the transport regimes of the SQD detector setup in the plane spanned by the detector bias voltage and the source chemical potential. The diagram reflects the interplay between the two relevant detector transport channels at energies ϵ_D and $\epsilon_D + U$, whose availability depends on the occupation of the target dot S.

When the source chemical potential satisfies $\mu_S < \epsilon_S$, the target dot remains predominantly empty. In this regime, the detector dot effectively behaves as an isolated single-level system at energy ϵ_D, and transport through the detector occurs only when ϵ_D lies within the bias window defined by μ_{D_L} and μ_{D_R}. Conversely, for $\mu_S > \epsilon_S + U$, the target dot is almost always occupied, shifting the effective detector level to $\epsilon_D + U$ and suppressing transport through the lower-energy channel.

In the intermediate regime $\epsilon_S < \mu_S < \epsilon_S + U$, the target dot is partially occupied. As a result, both detector channels contribute to transport, leading to a coexistence region in which the detector current reflects stochastic switching between the two Coulomb-shifted configurations. This conditional modulation of the detector conductance constitutes the basic charge-sensing mechanism in the SQD setup.

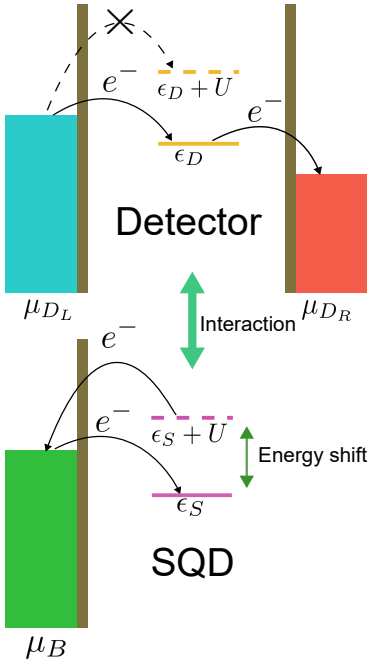

Figure 2.2: Schematic illustration of the coupled SQD–detector system. The detector is tunnel-coupled to two reservoirs with chemical potentials μ_L and μ_R, generating a current when its energy level falls within the transport window. Due to capacitive coupling, the detector/SQD energy level shifts by an interaction energy U depending on the occupation of the detector/SQD, enabling charge sensing through current modulation.

The detector current as a function of the bias voltage $V/U = (\mu_{D_L} - \mu_{D_R})/U$ is shown in Fig. 2.3 for several values of the source chemical potential μ_S. The current exhibits step-like features characteristic of sequential tunneling through discrete energy levels.

For values of μ_S such that the target dot remains empty, a single current step appears when the bias window opens around ϵ_D. When the target dot is occupied, the current onset is shifted to higher bias, corresponding to the Coulomb-shifted level $\epsilon_D + U$. In the intermediate regime of partial target-dot occupation, two current steps are observed, reflecting the simultaneous contribution of both transport channels.

These features demonstrate that the detector current is not determined solely by the applied bias, but is strongly influenced by the charge state of the target dot. The capacitive interaction thus converts charge fluctuations of the target into measurable current variations in the detector.

The effect of temperature on the transport characteristics is illustrated in Fig. 2.4, and the current and the differential conductance dI/dV are shown in Fig. 2.5 for moderate and low temperatures. At finite temperature, thermal broadening of the Fermi distributions allows partial occupation of the target dot even when μ_S is close to ϵ_S. As a result, the detector current displays two broadened steps and the differential conductance exhibits two finite peaks corresponding to the two transport channels.

In the low-temperature limit, the Fermi functions approach sharp step functions. Once $\mu_S > \epsilon_S + U$, the target dot becomes fully occupied, and transport through the lower-energy detector channel at ϵ_D is completely suppressed. This leads to a pronounced Coulomb blockade of the detector current and the disappearance of the corresponding conductance peak. The remaining current step at $\epsilon_D + U$ reflects transport through a single, interaction-shifted channel.

The sharpening of the conductance features at low temperature highlights the discrete nature of the transport channels and emphasizes the role of the Coulomb interaction in controlling

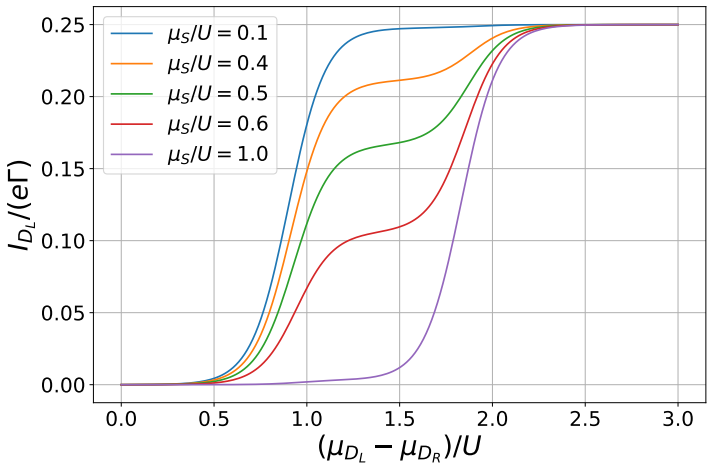

Figure 2.3: Current I_D vs $V/U = (\mu_{D_L} - \mu_{D_R})/U$, Other parameters are $\epsilon_D/U = 1$, $\epsilon_S/U = 0.5$, $\kappa_{D_L}/\Gamma = \kappa_{D_R}/\Gamma = 1/2$, and $\kappa_B/\Gamma = 2$.

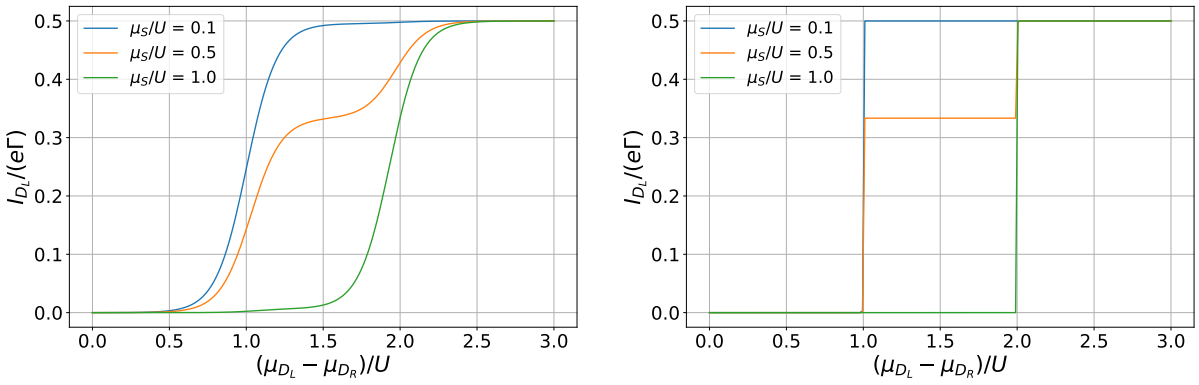

(a) $k_BT/U = 0.1$ (b) $k_BT/U = 10^{-5}$

Figure 2.4: Normalized detector current $I_{D_L}/(e\Gamma)$ as a function of the bias voltage $(\mu_{D_L} - \mu_{D_R})/U$ for several values of the source chemical potential μ_S/U. (a) $k_BT/U = 0.1$. (b) $k_BT/U = 10^{-5}$. The right detector chemical potential is fixed at $\mu_{D_R}/U = 0.1$, while μ_{D_L} is varied to generate the bias. Other parameters are $\epsilon_D/U = 1$, $\epsilon_S/U = 0.5$, $\kappa_{D_L}/\Gamma = \kappa_{D_R}/\Gamma = 0.5$, and $\kappa_B/\Gamma = 2$.

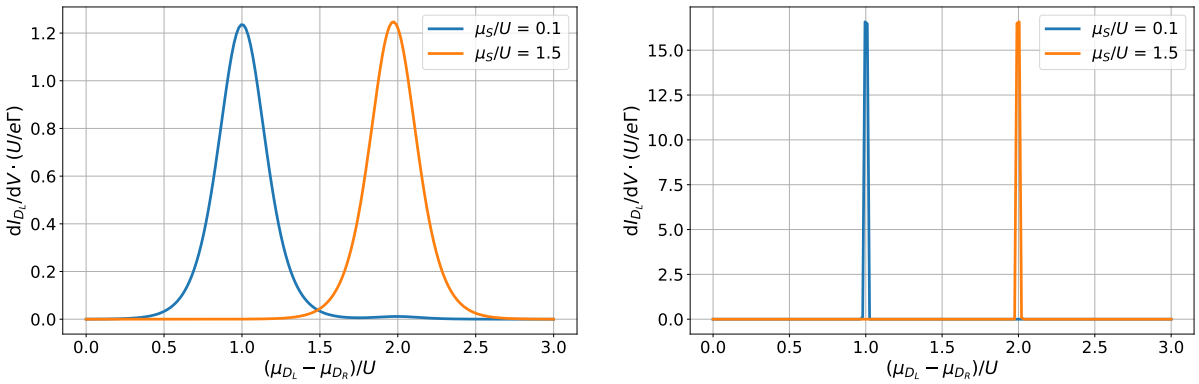

(a) $k_BT/U = 0.1$ (b) $k_BT/U = 10^{-5}$

Figure 2.5: Differential conductance dI_{D_L}/dV at moderate and near-zero temperatures. Other parameters are same as Fig. 2.4

detector conductance. In this regime, the SQD setup operates as an effective charge switch, where the occupation of the target dot deterministically enables or disables transport through the detector.

The results presented above illustrate that the SQD detector operates as a conditional conductor, whose transport properties depend explicitly on the charge configuration of a spatially separated quantum dot. Importantly, this behavior arises entirely from incoherent sequential tunneling processes and does not rely on quantum coherence or entanglement between the dots.

These results lead to two primary implications for the SQD sensing setup. First, the model demonstrates that the fundamental mechanism of charge sensing—namely, the conditional modulation of detector conductance—is effectively manifested through a classical stochastic evolution of occupation probabilities. This is consistent with the charge-diagonal structure of the master equation in the absence of coherent inter-dot tunneling. However, while this classical framework captures the dominant transport features observed in sequential tunneling, it remains a simplified description; in a realistic experimental environment, higher-order tunneling processes or non-Markovian environmental effects may introduce corrections not accounted for by this baseline model. Second, the SQD module provides a well-defined reference for identifying genuinely quantum-coherent effects in more complex configurations, such as the double quantum dot system treated in the next chapter.

In the next chapter, we extend the analysis to a double quantum dot system, where coherent inter-dot tunneling introduces superpositions between charge states. As will be shown, this qualitatively modifies the structure of the master equation and necessitates additional approximations beyond those employed in the SQD case.

3 Double Quantum Dot: Coherence and Detector Backaction

3.1 Motivation and Overview

Building on the classical sensing mechanism established in Chapter 2, this chapter extends our framework to a double quantum dot (DQD) system. The system consists of a detector quantum dot (D) biased by two electronic reservoirs, and a coherently coupled DQD (sites L and R) isolated from particle exchange. As illustrated in Fig. 3.1, the two subsystems interact solely through electrostatic capacitive couplings U_L and U_R, which shift the detector level conditionally based on the DQD charge configuration. Restricting the DQD to the single-excess-electron regime, it forms an effective two-level system where the electron can occupy coherent superpositions of the left and right states.

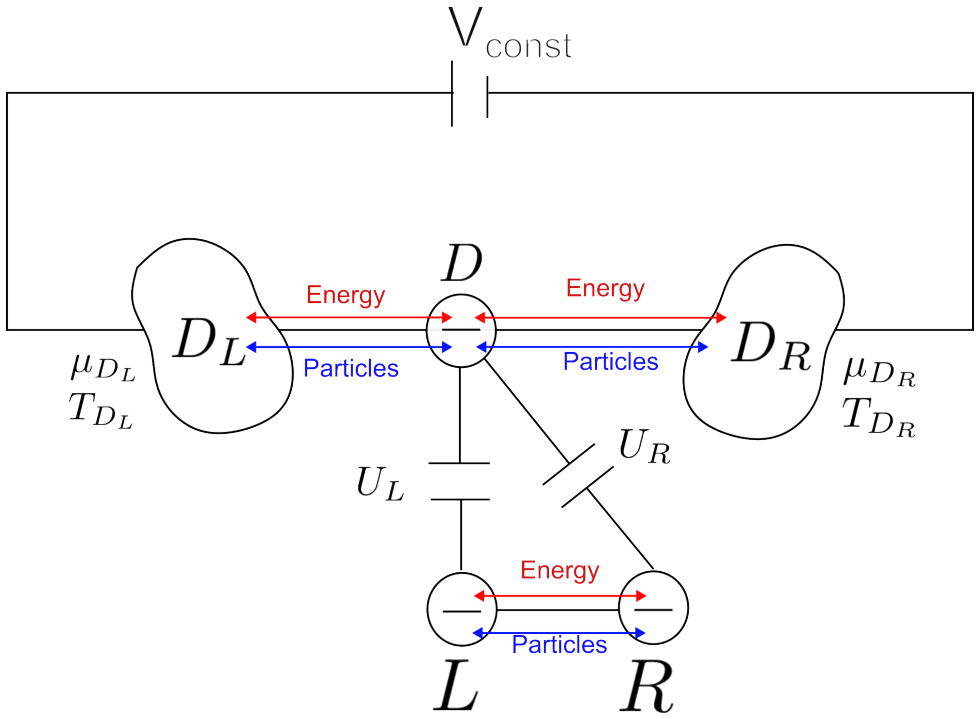

Figure 3.1: Double quantum dot (DQD) capacitively coupled to a quantum dot detector. The detector is tunnel-coupled to two reservoirs with chemical potentials μ_{D_L} and μ_{D_R}. The DQD is isolated from the reservoirs but supports coherent inter-dot tunneling with amplitude g.

We investigate the competition between coherent inter-dot tunneling and measurement-induced backaction. To achieve this, we follow a similar trajectory as in the previous chapter, including: (i) the derivation of a Markovian master equation for the coupled DQD-detector system under non-equilibrium bias, (ii) the evaluation of the steady-state detector current and the extraction of the effective dephasing rate, and (iii) the introduction of a time-scale separation (TSS) approach to analytically capture the effective DQD dynamics in the fast-detector limit.

The outputs of this chapter aim to identify the optimal operating regime for continuous charge sensing. In Chapter 2, we established that the device only functions as a valid detector within a specific bias voltage window where the current becomes highly sensitive to the target charge state. Comparison of the full Liouvillian solution with the TSS model shows that while the measurement information is exclusively extracted within this specific voltage window, the induced dephasing is actually not maximized there. This reveals that efficient charge detection can be achieved with a relatively low measurement backaction on the coherent quantum dynamics.

3.2 Model and Hamiltonian

Following the physical setting introduced above, we now formalize the model algebraically. The three relevant fermionic modes are described by the annihilation operators $\hat{d}_D$ (for the detector), and $\hat{d}_L, \hat{d}_R$ (for the left and right DQD sites). The total system Hamiltonian reads:

$$\hat{H}_S = \epsilon_D \hat{d}_D^\dagger \hat{d}_D + \epsilon_L \hat{d}_L^\dagger \hat{d}_L + \epsilon_R \hat{d}_R^\dagger \hat{d}_R + g\, \hat{d}_L^\dagger \hat{d}_R + g^*\, \hat{d}_R^\dagger \hat{d}_L + U_L \hat{d}_D^\dagger \hat{d}_D\, \hat{d}_L^\dagger \hat{d}_L + U_R \hat{d}_D^\dagger \hat{d}_D\, \hat{d}_R^\dagger \hat{d}_R. \quad (3.1)$$

The first three terms describe the on-site energies of the detector and the two DQD sites. The fourth and fifth terms represent coherent tunneling between the left and right dots of the DQD, with complex amplitude g. This term is responsible for coherent charge oscillations within the DQD.

The last two terms describe the capacitive coupling between the detector and the DQD. If the left (right) dot is occupied, the detector level is shifted by an energy U_L (U_R). Importantly, these interaction terms conserve particle number in each subsystem separately, reflecting the absence of direct tunneling between detector and DQD.

The detector dot is tunnel-coupled to two fermionic reservoirs,

$$H_\alpha = \sum_q \epsilon_{\alpha,q} \hat{c}_{\alpha,q}^\dagger \hat{c}_{\alpha,q}, \qquad \alpha = D_L, D_R, \quad (3.2)$$

with coupling Hamiltonian

$$V_\alpha = \sum_q \left(g_{\alpha,q} \hat{d}_D \hat{c}_{\alpha,q}^\dagger - g_{\alpha,q} \hat{d}_D^\dagger \hat{c}_{\alpha,q} \right). \quad (3.3)$$

The reservoirs are characterized by Fermi distributions

$$n_F^\alpha(\omega) = \frac{1}{e^{(\omega-\mu_\alpha)/k_B T} + 1}, \quad (3.4)$$

where μ_α and T denote chemical potential and temperature. A finite bias voltage $V = \mu_{D_L} - \mu_{D_R}$ drives transport through the detector.

The full Hilbert space of the coupled DQD–detector system is spanned by the occupation basis

$$|ijk\rangle = |i\rangle_D \otimes |j\rangle_L \otimes |k\rangle_R, \qquad i, j, k \in \{0, 1\}.$$

In principle, this yields eight basis states. While the full local occupation basis of the three modes contains $2^3 = 8$ states, the single-excess-electron restriction formally reduces the relevant DQD Hilbert space to the subspace spanned by:

$$|L\rangle \equiv |10\rangle_{LR}, \qquad |R\rangle \equiv |01\rangle_{LR}.$$

Within this subspace, coherent superpositions $a|L\rangle + b|R\rangle$ are allowed and play a central role in

the following analysis.

The detector occupation $\hat{n}_D = \hat{d}_D^\dagger \hat{d}_D$ remains dynamical due to its coupling to the reservoirs. Consequently, the dynamics of the full system involves both coherent DQD oscillations and dissipative detector tunneling processes.

Throughout this chapter, all energies (including dot levels $\epsilon_D, \epsilon_{L,R}$, charging energies $U_{L,R}$, and chemical potentials $\mu_{D_{L,R}}$), as well as the inter-dot coupling g and tunneling rates $\kappa_{D_{L,R}}$, are expressed in the same energy units. To facilitate comparison across different parameter sets in our numerical results, these quantities are typically scaled by a characteristic energy, such as the left capacitive coupling U_L.

3.3 Master equation for the coupled DQD–detector system

We now derive the Markovian master equation describing the dynamics of the coupled DQD–detector system under non-equilibrium bias.

Following the standard derivation outlined in Chapter 2, we assume weak coupling between the detector dot and its reservoirs. Under the Born approximation, the total density matrix factorizes as

$$\hat{\rho}_{\text{tot}}(t) \simeq \hat{\rho}_S(t) \otimes \hat{\rho}_{D_L} \otimes \hat{\rho}_{D_R}, \tag{3.5}$$

where each reservoir remains in thermal equilibrium,

$$\hat{\rho}_\alpha = \frac{e^{-\beta(\hat{H}_\alpha - \mu_\alpha \hat{N}_\alpha)}}{\text{Tr}[e^{-\beta(\hat{H}_\alpha - \mu_\alpha \hat{N}_\alpha)}]}, \qquad \alpha = D_L, D_R. \tag{3.6}$$

The Markov approximation further assumes that reservoir correlation functions decay on a time scale much shorter than the intrinsic system dynamics. As in Chapter 2, this leads to a time-local master equation for the reduced density matrix $\hat{\rho}_S(t)$.

The interaction Hamiltonian can be written in the standard form

$$\hat{H}_{int} = \sum_{\alpha = D_L, D_R} \left(\hat{S}_{\alpha,0} \otimes \hat{B}_{\alpha,0} + \hat{S}_{\alpha,1} \otimes \hat{B}_{\alpha,1} \right), \tag{3.7}$$

with system operators

$$\hat{S}_{\alpha,0} = \hat{d}_D, \qquad \hat{S}_{\alpha,1} = \hat{d}_D^\dagger. \tag{3.8}$$

In the interaction picture,

$$\tilde{S}_{\alpha,k}(t) = e^{i\hat{H}_S t} \hat{S}_{\alpha,k} e^{-i\hat{H}_S t}. \tag{3.9}$$

Because the detector level is shifted by the DQD occupations through the interaction terms $U_L \hat{n}_D \hat{n}_L + U_R \hat{n}_D \hat{n}_R$, the time evolution of $\hat{d}_D$ depends on the DQD charge configuration. Using the Baker–Campbell–Hausdorff expansion (Appendix A), we obtain

$$\begin{aligned} \tilde{S}_{\alpha,0}(t) = {} & e^{-i\epsilon_D t} \hat{d}_D (1 - \hat{n}_L)(1 - \hat{n}_R) \\ & + e^{-i(\epsilon_D + U_L)t} \hat{d}_D \hat{n}_L (1 - \hat{n}_R) \\ & + e^{-i(\epsilon_D + U_R)t} \hat{d}_D (1 - \hat{n}_L) \hat{n}_R \\ & + e^{-i(\epsilon_D + U_L + U_R)t} \hat{d}_D \hat{n}_L \hat{n}_R. \end{aligned} \tag{3.10}$$

Each term corresponds to a detector tunneling event conditioned on the occupation state of the DQD. The four possible Bohr frequencies are therefore

$$\omega_1 = \epsilon_D, \quad \omega_2 = \epsilon_D + U_L, \quad \omega_3 = \epsilon_D + U_R, \quad \omega_4 = \epsilon_D + U_L + U_R. \tag{3.11}$$

However, as established in Sec. 3.2, the strong Coulomb blockade restricts the DQD to the single-excess-electron subspace spanned by $\{|L\rangle, |R\rangle\}$. Consequently, the probability of finding the DQD completely empty ($n_L = n_R = 0$) or doubly occupied ($n_L = n_R = 1$) is strictly zero. The jump operators associated with ω_1 and ω_4 vanish within the single-excess-electron subspace when acting on the relevant reduced density matrix, and we only retain the conditional transport channels corresponding to $\epsilon_D + U_L$ and $\epsilon_D + U_R$.

The derivation of the master equation proceeds analogously to the single-dot case in Sec. 2.3. However, in contrast to the single-dot setup, the DQD supports coherent superpositions between $|L\rangle$ and $|R\rangle$. Because the reduced density matrix $\hat{\rho}_S(t)$ now contains non-zero off-diagonal coherences in the charge basis, the cross-terms in the dissipator associated with different Bohr frequencies, such as $\hat{n}_L\hat{\rho}_S(t)\hat{n}_R$ in the master equation, no longer evaluate to zero identically. These terms, oscillating at frequencies $e^{\pm i(U_L-U_R)t}$, would continuously couple different transition channels and prevent a time-independent GKLS structure. We therefore apply the secular approximation by explicitly dropping all terms with $j \neq j'$ in the analogue of Eq. (2.22). Physically, this is justified when the detector's characteristic relaxation rates are much smaller than the conditional energy splitting, satisfying the inequality $\kappa_\alpha \ll |U_L - U_R|$. The resulting completely positive master equation in the Schrödinger picture reads:

$$\partial_t\hat{\rho}_S = -i[\hat{H}_S, \hat{\rho}_S] + \sum_{\alpha=D_L,D_R}\sum_{\beta=L,R}\left(\Gamma^0_{\alpha,\beta}\mathcal{D}[\hat{d}_D\hat{n}_\beta] + \Gamma^1_{\alpha,\beta}\mathcal{D}[\hat{d}^\dagger_D\hat{n}_\beta]\right)\hat{\rho}_S, \tag{3.12}$$

where

$$\Gamma^0_{\alpha,\beta} = \kappa_\alpha\left[1 - n^\alpha_F(\epsilon_D + U_\beta)\right], \qquad \Gamma^1_{\alpha,\beta} = \kappa_\alpha n^\alpha_F(\epsilon_D + U_\beta), \tag{3.13}$$

and $\mathcal{D}[\hat{O}]\rho = \hat{O}\rho\hat{O}^\dagger - \frac{1}{2}\{\hat{O}^\dagger\hat{O}, \rho\}$.

3.4 Full system dynamics and detector current

The charge detector is operated under a finite bias $V = \mu_{D_L} - \mu_{D_R}$, which drives a stationary particle current through the detector dot. To characterize this transport response in a dimensionless form, we normalize the detector current by the total bare tunneling rate of the detector,

$$\Gamma \equiv \kappa_{D_L} + \kappa_{D_R}. \tag{3.14}$$

The dimensionless steady-state current is thus defined as $\tilde{I}_{D_L} \equiv I_{D_L}/(e\Gamma)$. In the following, we first derive the exact expression for I_{D_L} from the master equation and subsequently evaluate its dependence on the applied bias.

Following the general trace formalism introduced in Sec. 2.4 for evaluating particle flux, the specific steady-state current for our coupled DQD-detector system is obtained by tracing over the relevant jump operators. By utilizing the state-dependent tunneling rates $\Gamma^{0/1}_{L,R}$ derived in Sec. 3.3, the current flowing from the left lead into the detector is explicitly given by:

$$I_{D_L} = -e\sum_{\beta=L,R}\left[\Gamma^1_{D_L,\beta}\,P_{0,\beta} - \Gamma^0_{D_L,\beta}\,P_{1,\beta}\right]. \tag{3.15}$$

where we have introduced the detector-resolved populations of the DQD,

$$P_{n_D,\beta} \equiv \langle n_D, \beta|\hat{\rho}_S|n_D, \beta\rangle. \tag{3.16}$$

Here, $n_D \in \{0, 1\}$ denotes the detector occupation and $\beta \in \{L, R\}$ labels the relevant DQD charge localization states, $|L\rangle \equiv |10\rangle_{LR}$ and $|R\rangle \equiv |01\rangle_{LR}$. The first term describes injection events from D_L into the detector (weighted by the probability that the detector is empty),

and the second term describes extraction events from the detector into D_L (weighted by the probability that the detector is occupied). The dependence on β encodes the fact that the effective detector level, and hence the tunneling rates depend on the DQD charge configuration through the capacitive coupling.

Figs. 3.2a and 3.2b show the detector I–V curves computed for two different temperatures, $k_BT/U_L = 10^{-1}$ and $k_BT/U_L = 10^{-3}$, while keeping the remaining parameters fixed. The qualitative role of temperature is to control the sharpness of the Fermi edges in the reservoirs and thereby the effective broadening of detector transport thresholds. At the higher temperature (Fig. 3.2a), the same onsets are thermally smeared: the current steps broaden and the contrast between conditional channels is reduced. At very low temperature (Fig. 3.2b), the current exhibits sharp step-like onsets as a function of bias, reflecting well-resolved transport channels associated with the conditional detector energies $\epsilon_D + U_L$ and $\epsilon_D + U_R$.

This trend mirrors the temperature dependence observed for the single-dot detector model in Chapter 2, but here it occurs in the presence of a coherently evolving DQD target.

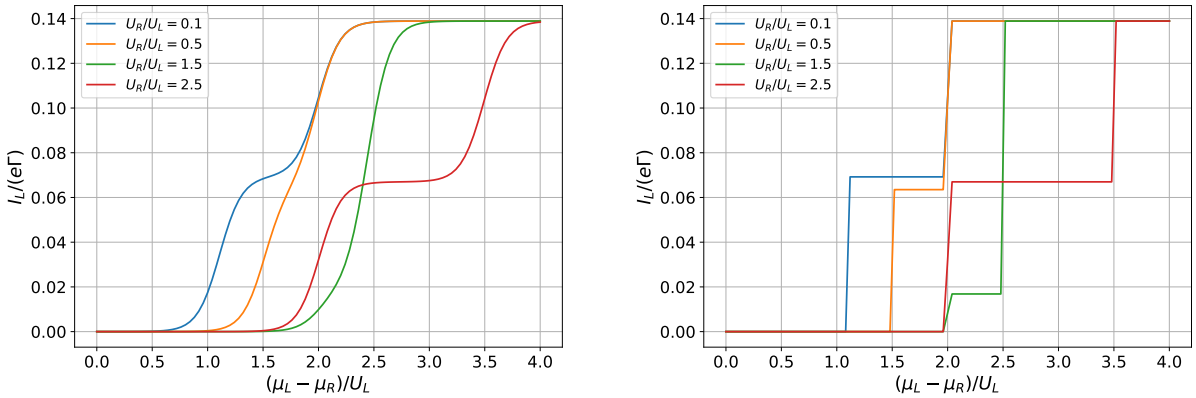

(a) $k_BT/U_L = 10^{-1}$ (b) $k_BT/U_L = 10^{-3}$

Figure 3.2: Detector I–V characteristics at different temperature with the same parameters. The right detector chemical potential is fixed at $\mu_{D_R}/U_L = 0.1$, while μ_{D_L} is varied to generate the bias. Other parameters are $\epsilon_D/U_L = 1.0$, $\epsilon_L/U_L = 0.5$, $\epsilon_R/U_L = 0.1$, $g/U_L = 0.1$, $\kappa_{D_L}/\Gamma = \kappa_{D_R}/\Gamma = 0.5$.

To isolate the effect of coherent inter-dot tunneling, Fig. 3.3 compares three representative curves: (i) a stationary I–V curve obtained for a coherently coupled DQD ($g \neq 0$), and (ii) two reference curves corresponding to the limit $g = 0$, where the excess electron is fixed on the left dot ($|L\rangle$) or on the right dot ($|R\rangle$). In the strictly static case $g = 0$, the detector responds to a *classical* charge configuration of the DQD, and the current traces therefore reflect two distinct conditional detector channels. When $g \neq 0$, by contrast, the DQD can occupy coherent superpositions of $|L\rangle$ and $|R\rangle$, and the detector backaction (dephasing and measurement-induced modification of the DQD dynamics) feeds back into the stationary populations entering Eq. (3.15).

For $g \neq 0$, the stationary current can be obtained by solving the linear steady-state condition $\mathcal{L}[\rho_S^{\rm ss}] = 0$ together with $\mathrm{Tr}\rho_S^{\rm ss} = 1$. In the special limit $g = 0$, however, the Liouvillian decomposes into disconnected invariant subspaces associated with fixed DQD charge localization, and the stationary solution is not unique unless an initial condition is specified. For this reason, we evaluate the $g = 0$ reference curves by time-evolving the master equation from initial states $|L\rangle$ and $|R\rangle$ and extracting the long-time limit of the current, which selects the physically relevant steady state for the chosen preparation.

By solving the stationary condition $\mathcal{L}[\rho_S^{\rm ss}] = 0$, we obtain the steady-state current I_{D_L} as

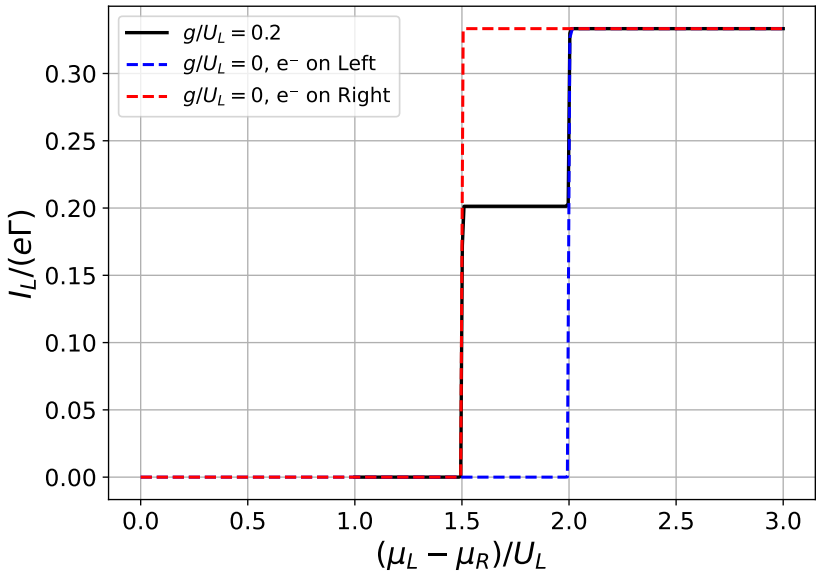

Figure 3.3: Comparison of detector I–V curves for $g \neq 0$ (coherent DQD) and for $g = 0$ with the electron prepared on the left ($|L\rangle$) or right ($|R\rangle$) dot. The $g = 0$ curves are obtained from long-time propagation to select the steady state corresponding to a given initial localization, whereas the $g \neq 0$ curve is obtained from the unique stationary solution of the full Liouvillian. The deviation between $g \neq 0$ and $g = 0$ highlights detector backaction in the coherent regime. Other parameters are the same as Fig. 3.2

a function of the applied bias V. As shown in Fig. 3.2, the current exhibits distinct transport thresholds set by the conditional detector energies. For biases below the lowest threshold, transport is suppressed due to Coulomb blockade. As the bias increases, two successive onsets appear, corresponding to the channels at $\epsilon_D + U_L$ and $\epsilon_D + U_R$.

In the intermediate bias window between these two thresholds, the current depends strongly on the DQD charge configuration. For larger biases, where both channels lie within the transport window, the current becomes independent of the DQD state.

While the full master equation provides an exact numerical description of the stationary current, the measurement-induced backaction is encoded implicitly in the coupled detector dynamics. To obtain a reduced description of the effective DQD dynamics and an analytical expression for the induced dephasing, we now introduce a time-scale separation (TSS) approach, valid in the regime where detector relaxation is fast compared to the coherent inter-dot tunneling.

3.5 Time-scale separation and effective DQD dynamics

The full master equation derived in Sec. 3.3 describes the coupled dynamics of three fermionic modes: the detector dot D and the two DQD sites L and R. While this description is exact within the Born–Markov and secular approximations, it contains both fast and slow processes. In particular, the detector dot is tunnel-coupled to two reservoirs with rates κ_{D_L} and κ_{D_R}, whereas the intrinsic DQD dynamics is governed by the coherent inter-dot coupling g.

We consider the regime

$$\kappa_{D_L}, \kappa_{D_R} \gg |g|, \tag{3.17}$$

in which the detector relaxes much faster than the DQD evolves coherently. Physically, this corresponds to a strongly coupled charge detector that rapidly equilibrates for any instanta-

neous DQD configuration. The detector therefore acts as a fast subsystem, whereas the DQD populations evolve on a slower time scale.

This hierarchy allows us to eliminate the fast detector degrees of freedom and derive an effective reduced dynamics for the DQD alone.

We work within the single-charge manifold of the DQD, spanned by the basis $\{|L\rangle, |R\rangle\}$ corresponding to one excess electron localized on either dot. Within this subspace, the dynamics include both charge populations and their quantum coherence.

We use the populations $P_{i,L}, P_{i,R}$ defined in Eq. (3.16) and introduce the coherences, defined as

$$\alpha_i \equiv \langle i, L|\hat{\rho}_S|i, R\rangle. \tag{3.18}$$

Here, $i \in \{0, 1\}$ denoting the detector occupation. The equations of motion take the form

$$\partial_t P_{i,L} = -i(g^*\alpha_i^* - g\alpha_i) + \sum_{\alpha=D_L,D_R} \left(\Gamma^i_{\alpha,L} P_{\bar{i},L} - \Gamma^{\bar{i}}_{\alpha,L} P_{i,L}\right), \tag{3.19}$$

$$\partial_t P_{i,R} = +i(g^*\alpha_i^* - g\alpha_i) + \sum_{\alpha=D_L,D_R} \left(\Gamma^i_{\alpha,R} P_{\bar{i},R} - \Gamma^{\bar{i}}_{\alpha,R} P_{i,R}\right), \tag{3.20}$$

$$\partial_t \alpha_i = -i\Delta_i \alpha_i - ig^*(P_{i,R} - P_{i,L}) - \frac{1}{2}\sum_{\alpha,\beta} \Gamma^{\bar{i}}_{\alpha,\beta}\alpha_i, \tag{3.21}$$

where $\bar{i} = 1 - i$ and $\Delta_i = E_{i,L} - E_{i,R}$ denotes the detector-conditioned energy detuning.

On time scales short compared to $1/|g|$, the coherent inter-dot coupling can be neglected. Setting $g = 0$ in the population equations yields fast relaxation within each DQD subspace. Imposing $\partial_t P_{i,L} = 0$ for fixed $P_L = P_{0,L} + P_{1,L}$ gives

$$P_{i,L} = \tau_{i,L} P_L, \qquad \tau_{i,L} = \frac{\sum_\alpha \Gamma^i_{\alpha,L}}{\sum_\alpha \Gamma^0_{\alpha,L} + \sum_\alpha \Gamma^1_{\alpha,L}}. \tag{3.22}$$

An analogous expression holds for $P_{i,R}$. Thus, the detector occupation instantaneously follows the DQD configuration through conditional steady-state occupancy probabilities $\tau_{i,\beta}$.

The coherences α_i are damped by both energy detuning and detector-induced dephasing. Under the time-scale separation condition (3.17), they relax rapidly compared to the slow evolution of P_L and P_R. We therefore impose $\partial_t \alpha_i \simeq 0$ in Eq. (3.21), which yields

$$\alpha_i = \frac{g^*(P_{i,L} - P_{i,R})}{\Delta_i + \frac{i}{2}\sum_{\alpha,\beta} \Gamma^{\bar{i}}_{\alpha,\beta}}. \tag{3.23}$$

Substituting this expression back into the population equations, the coherent term $-i(g^*\alpha_i^* - g\alpha_i)$ reduces to an effective incoherent transition term of order $|g|^2$:

$$-i(g^*\alpha_i^* - g\alpha_i) = -\gamma_i |g|^2 (P_{i,L} - P_{i,R}), \tag{3.24}$$

where the effective rate is

$$\gamma_i = \frac{\sum_{\alpha,\beta} \Gamma^{\bar{i}}_{\alpha,\beta}}{\frac{1}{4}\left(\sum_{\alpha,\beta} \Gamma^{\bar{i}}_{\alpha,\beta}\right)^2 + \Delta_i^2}. \tag{3.25}$$

Summing over detector occupations and defining $P_L = \sum_i P_{i,L}, \quad P_R = \sum_i P_{i,R}$, we obtain

a closed classical master equation

$$\partial_t \begin{pmatrix} P_L \\ P_R \end{pmatrix} = \begin{pmatrix} -k_{L\to R} & k_{R\to L} \\ k_{L\to R} & -k_{R\to L} \end{pmatrix} \begin{pmatrix} P_L \\ P_R \end{pmatrix}, \tag{3.26}$$

with

$$k_{L\to R} = |g|^2 \left(\gamma_0 \tau_{0,L} + \gamma_1 \tau_{1,L}\right), \qquad k_{R\to L} = |g|^2 \left(\gamma_0 \tau_{0,R} + \gamma_1 \tau_{1,R}\right). \tag{3.27}$$

The time-scale separation procedure shows that coherent inter-dot tunneling with amplitude g is converted into an effective classical transition process between the left and right dots, with rate proportional to $|g|^2$ and suppressed by detector-induced dephasing. In this picture, the detector acts as a continuous measurement device: it monitors the DQD charge configuration and induces dephasing that competes with coherent oscillations.

Summing the two equations in Eq. (3.26) yields

$$\partial_t (P_L + P_R) = 0 \quad \Rightarrow \quad P_L(t) + P_R(t) = 1, \tag{3.28}$$

so the reduced dynamics remains normalized.

Using $P_R(t) = 1 - P_L(t)$, Eq. (3.26) reduces to

$$\dot{P}_L(t) = -(k_{L\to R} + k_{R\to L}) P_L(t) + k_{R\to L}. \tag{3.29}$$

Solving this linear equation gives

$$P_L(t) = P_L^{\text{ss}} + \left(P_L(0) - P_L^{\text{ss}}\right) e^{-(k_{L\to R} + k_{R\to L})t}, \qquad P_R(t) = 1 - P_L(t), \tag{3.30}$$

with steady-state populations

$$P_L^{\text{ss}} = \frac{k_{R\to L}}{k_{L\to R} + k_{R\to L}}, \qquad P_R^{\text{ss}} = \frac{k_{L\to R}}{k_{L\to R} + k_{R\to L}}. \tag{3.31}$$

The relaxation time of the slow dynamics is therefore

$$\tau_{\text{slow}} = \frac{1}{k_{L\to R} + k_{R\to L}}. \tag{3.32}$$

Within the TSS description, the detector current (see Eq. (3.15)) from the left lead reads

$$I_{D_L}(t) = -e\Big[\Gamma^1_{D_L,R}\tau_{0,R} P_R(t) + \Gamma^1_{D_L,L}\tau_{0,L} P_L(t) - \Gamma^0_{D_L,R}\tau_{1,R} P_R(t) - \Gamma^0_{D_L,L}\tau_{1,L} P_L(t)\Big]. \tag{3.33}$$

In steady state, inserting Eq. (3.31) yields the closed expression

$$I^{\text{ss}}_{D_L}(V) = -e \frac{A_R(V)\, k_{L\to R}(V) + A_L(V)\, k_{R\to L}(V)}{k_{L\to R}(V) + k_{R\to L}(V)}, \tag{3.34}$$

where

$$A_R(V) = \Gamma^1_{D_L,R}\tau_{0,R} - \Gamma^0_{D_L,R}\tau_{1,R}, \qquad A_L(V) = \Gamma^1_{D_L,L}\tau_{0,L} - \Gamma^0_{D_L,L}\tau_{1,L}. \tag{3.35}$$

To rigorously justify the validity of this TSS approximation, in Fig. 3.4, we compare the detector current derived above with the numerical solution obtained from the full Liouvillian.

The TSS description is valid as long as the detector relaxation rates dominate over the coherent coupling, $|g| \ll \kappa_{D_L}, \kappa_{D_R}$. When $|g|$ becomes comparable to the detector relaxation rates, the full master equation must be used to capture coherent oscillations and their feedback on transport. Having validated the TSS framework through the steady-state transport, we can

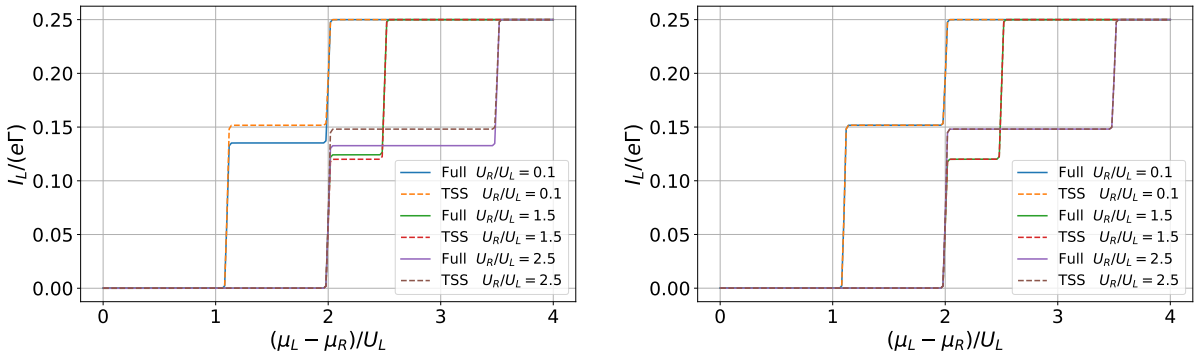

(a) (b)

Figure 3.4: Comparison of the steady-state detector current I_{D_L} obtained from the full master equation (solid lines) and the analytical time-scale separation (TSS) approach (dashed lines). (a) Current evaluated outside the strict TSS limit ($|g|$ is comparable to $\kappa_{D_L}, \kappa_{D_R}$), showing visible deviations due to the feedback of coherent oscillations on transport. (b) Current evaluated in the fast-detector limit ($|g| \ll \kappa_{D_L}, \kappa_{D_R}$), demonstrating excellent quantitative agreement.

now use this reduced description to explicitly extract the measurement-induced dephasing rate, a task we shall undertake in Sec. 3.6

3.6 Effective Dephasing Rate

In the time–scale separation (TSS) regime, the detector acts as a fast environment for the DQD and induces a strong suppression of the inter-dot coherence. To quantify this measurement backaction in a compact way, we extract an *effective dephasing strength* by the slow DQD populations obtained from the TSS effective dynamics.

From the population–coherence equations in Sec. 3.3, the coherence α_i in detector occupation $i \in \{0, 1\}$ obeys Eq. (3.21). Here we define the total tunneling rate out of the current detector occupation as:

$$\Lambda_i \equiv \sum_{\alpha \in \{D_L, D_R\}} \sum_{\beta \in \{L,R\}} \Gamma^{\bar{i}}_{\alpha,\beta}. \tag{3.36}$$

where $\bar{i} = 1 - i$ denotes the complementary detector occupation. With this shorthand, Eq. (3.21) becomes

$$\partial_t \alpha_i = -i\Delta_i\, \alpha_i - ig^*(P_{i,R} - P_{i,L}) - \frac{\Lambda_i}{2}\, \alpha_i. \tag{3.37}$$

Given the fluctuations in detector occupation, the DQD dynamics are distributed across the occupations $i = 0, 1$ according to the probabilities $P_i(t) = P_{i,L}(t) + P_{i,R}(t)$. We therefore define the effective measurement-induced dephasing strength as the average of the population probabilities

$$\tilde{\Gamma}(t) \equiv \sum_{i=0,1} P_i(t)\, \Lambda_i, \qquad P_i(t) = P_{i,L}(t) + P_{i,R}(t). \tag{3.38}$$

This definition captures the intuitive idea that the instantaneous coherence decay rate depends on the occupation of the detector the system occupies, and the observed dephasing is an average over these occupations.

Under the time-scale separation condition $\kappa_{D_L}, \kappa_{D_R} \gg |g|$, the detector relaxes rapidly to its conditional steady state for a fixed DQD configuration. As derived in Sec. 3.5, this leads to the factorization $P_{i,L}(t) = \tau_{i,L}\, P_L(t)$, $P_{i,R}(t) = \tau_{i,R}\, P_R(t)$, where $P_L(t) = \sum_i P_{i,L}(t)$ and

$P_R(t) = \sum_i P_{i,R}(t)$ are the slow DQD populations, and the conditional occupancy probabilities are derived above, see Eq.(3.22) and $\tau_{i,R}$ is analogous to $\tau_{i,L}$. Using Eq. (3.22), the probabilities for detector charge occupation become

$$P_i(t) = P_{i,L}(t) + P_{i,R}(t) = \tau_{i,L} P_L(t) + \tau_{i,R} P_R(t). \tag{3.39}$$

Substituting Eq. (3.39) into the definition Eq. (3.38) yields the closed expression

$$\tilde{\Gamma}(t) = \sum_{i=0,1} \big(\tau_{i,L} P_L(t) + \tau_{i,R} P_R(t)\big)\Lambda_i. \tag{3.40}$$

This shows that, within TSS, the time dependence of the dephasing strength is fully controlled by the slow two-state dynamics of $P_L(t)$ and $P_R(t)$.

Substituting Eq. (3.30) into Eq. (3.40) gives an explicit closed form:

$$\begin{aligned}
\tilde{\Gamma}(t) &= \sum_{i=0,1} \Big[\tau_{i,L} P_L(t) + \tau_{i,R}\big(1 - P_L(t)\big)\Big]\Lambda_i \\
&= \sum_{i=0,1} \Big[\tau_{i,R} + (\tau_{i,L} - \tau_{i,R}) P_L(t)\Big]\Lambda_i \\
&= \sum_{i=0,1} \Big[\tau_{i,R} + (\tau_{i,L} - \tau_{i,R})\Big(P_L^{\mathrm{ss}} + \big(P_L(0) - P_L^{\mathrm{ss}}\big) e^{-(k_{L\to R} + k_{R\to L})t}\Big)\Big]\Lambda_i.
\end{aligned} \tag{3.41}$$

This expression makes explicit that $\tilde{\Gamma}(t)$ relaxes exponentially to its steady value on the same slow time scale τ_{slow}.

Taking $t \to \infty$ in Eq. (3.41) yields

$$\begin{aligned}
\tilde{\Gamma}^{\mathrm{ss}} &= \sum_{i=0,1} \Big[\tau_{i,L} P_L^{\mathrm{ss}} + \tau_{i,R} P_R^{\mathrm{ss}}\Big]\Lambda_i \\
&= \sum_{i=0,1} \left(\tau_{i,L} \frac{k_{R\to L}}{k_{L\to R} + k_{R\to L}} + \tau_{i,R} \frac{k_{L\to R}}{k_{L\to R} + k_{R\to L}}\right)\Lambda_i,
\end{aligned} \tag{3.42}$$

which is the analytical TSS prediction for the bias-dependent dephasing strength once the voltage dependence of the rates is inserted.

The detector-induced rates entering Λ_i inherit their bias dependence through the Fermi functions of the detector reservoirs. With

$$\Gamma^0_{\alpha,\beta} = \kappa_\alpha \big[1 - n_F^\alpha(\epsilon_D + U_\beta)\big], \qquad \Gamma^1_{\alpha,\beta} = \kappa_\alpha\, n_F^\alpha(\epsilon_D + U_\beta), \tag{3.43}$$

and $\bar{i} = 1 - i$, Eq. (3.36) gives

$$\Lambda_0 = \sum_{\alpha\in\{D_L,D_R\}} \sum_{\beta\in\{L,R\}} \Gamma^1_{\alpha,\beta} = \sum_{\alpha\in\{D_L,D_R\}} \kappa_\alpha \sum_{\beta\in\{L,R\}} n_F^\alpha(\epsilon_D + U_\beta), \tag{3.44}$$

$$\Lambda_1 = \sum_{\alpha\in\{D_L,D_R\}} \sum_{\beta\in\{L,R\}} \Gamma^0_{\alpha,\beta} = \sum_{\alpha\in\{D_L,D_R\}} \kappa_\alpha \sum_{\beta\in\{L,R\}} \big[1 - n_F^\alpha(\epsilon_D + U_\beta)\big]. \tag{3.45}$$

Consequently, both $\tilde{\Gamma}^{\mathrm{ss}}(V)$ and the effective transition rates $k_{L\to R}(V), k_{R\to L}(V)$ acquire a characteristic step-like dependence on the bias through the reservoir occupations n_F^α.

The effective dephasing strength $\tilde{\Gamma}^{\mathrm{ss}}(V)$ derived above is not an abstract quantity, but linked to the transport properties of the detector. In particular, both the steady-state current and the

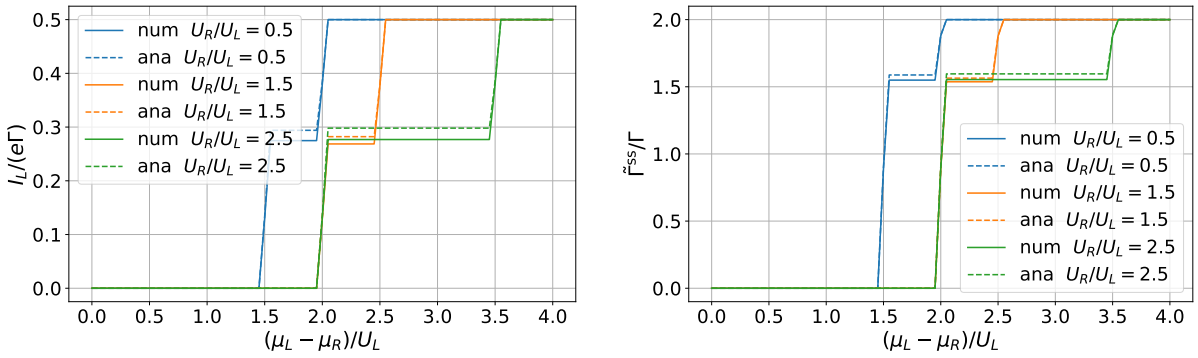

(a) (b)

Figure 3.5: Comparison between steady-state detector current and effective dephasing rate. (a) Steady-state current $I^{ss}_{D_L}$ and (b) effective dephasing rate $\tilde{\Gamma}^{ss}$ as a function of the bias voltage V (in units of U_L). Solid lines represent the numerical results from the full master equation, while dashed lines correspond to the analytical TSS expressions derived in Eq. (3.15) and Eq. (3.42). The two transport thresholds associated with the conditional detector levels $\epsilon_D + U_L$ and $\epsilon_D + U_R$ are clearly visible in both panels. Parameters: $g = 0.01$, $\kappa_{D_L}/\Gamma = \kappa_{D_R}/\Gamma = 0.5$, $\epsilon_D/\Gamma = 1$, $\epsilon_L/\Gamma = 0.5$, $\epsilon_R/\Gamma = 0.1$, $k_BT/U_L = 5 \times 10^{-3}$,

dephasing strength are controlled by the same voltage-dependent tunneling rates $\Gamma^{0/1}_{\alpha,\beta}$ through the Fermi functions $n^{\alpha}_F(\epsilon_D + U_\beta)$.

For larger inter-dot coupling g, coherent oscillations modify the steady-state populations, leading to visible deviations between the full and reduced descriptions. Comparing $I^{ss}_{D_L}(V)$ and $\tilde{\Gamma}^{ss}(V)$ in Fig. 3.5 shows that both quantities are set by the same voltage-dependent rates $\Gamma^{0/1}_{\alpha,\beta}$. The current is most sensitive to the DQD charge configuration in the bias range between the two transport thresholds associated with the conditional detector energies $\epsilon_D + U_L$ and $\epsilon_D + U_R$. However, $\tilde{\Gamma}^{ss}(V)$ does not necessarily peak in the same bias range. Within the present TSS description, $\tilde{\Gamma}^{ss}$ is controlled by the total tunneling rates entering Λ_i, whereas the stationary current depends on the imbalance between injection and extraction processes. This identifies operating points where charge sensitivity is substantial while the induced dephasing remains comparatively weak.

Compared to the theoretical model used in Ref. [10], our description makes the detector response explicitly state dependent. In the model of Ref. [10] (see Supplemental Material), the detector backaction is captured through charge-induced detuning fluctuations, while the detector transport is treated to leading order as independent of the instantaneous DQD charge configuration. In contrast, our Markovian treatment keeps the conditional detector tunneling channels associated with $\epsilon_D + U_L$ and $\epsilon_D + U_R$, such that both the stationary current and the effective dephasing measure $\tilde{\Gamma}^{ss}(V)$ are governed by the same set of state-dependent rates $\Gamma^{0/1}_{\alpha,\beta}$.

This additional feedback mechanism leads to a bias dependence of $\tilde{\Gamma}^{ss}(V)$ that can deviate from a simple scaling with the net detector current, and it naturally allows regimes in which the detector current changes while the induced dephasing varies only weakly.

As shown in Fig. 3.6, the resulting steady-state dephasing rate exhibits a monotonic linear dependence on the detector current over the considered bias range. This behavior is consistent with the experimentally observed scaling reported in Ref. [10], in particular with the linear fit to the decoherence rate as a function of current. A quantitative comparison requires device-specific parameters and goes beyond the scope of the present work, but the qualitative trends indicate that including the DQD-state dependence is important for capturing the structure of

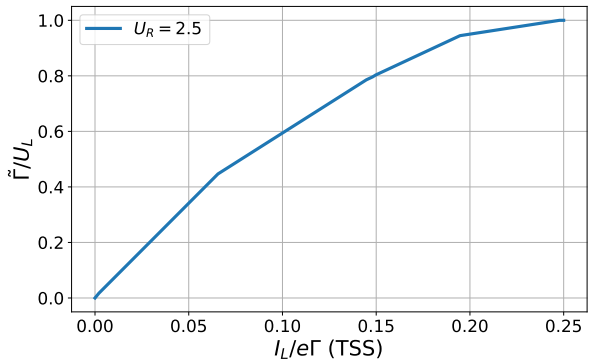

Figure 3.6: Steady-state dephasing rate $\tilde{\Gamma}^{\mathrm{ss}}$ as a function of the detector current I_d. The numerical results (dots) show a monotonic increase, consistent with the experimental trend and the linear fit reported in Ref. [10].

measurement backaction.

4 Discussion and Conclusions

Summary of the Present Work. In this thesis, we have developed a microscopic transport model for a double quantum dot (DQD) capacitively coupled to a continuously biased charge detector. The motivation of this work was to provide a self-consistent theoretical framework for understanding measurement-induced decoherence in continuous charge sensing experiments.

In Chapter 2, we first analyzed a single quantum dot (SQD) detector coupled to fermionic reservoirs. Starting from a Born–Markov master equation, we derived a time-local GKLS generator and established the voltage dependence of the detector current. This part served two purposes: (i) to benchmark the transport description, and (ii) to clarify how detector tunneling processes generate state-dependent jump operators through capacitive interactions.

In Chapter 3, we extended the analysis to the full DQD–detector system. We derived the master equation for the coupled three-mode system (detector dot D and DQD sites L and R), and studied both the steady-state transport properties and the effective dephasing induced by continuous measurement. We compared two levels of description: the full Liouvillian solution and a reduced time-scale separation (TSS) approach. This allowed us to identify the parameter regime in which the detector acts as a fast subsystem that converts coherent inter-dot tunneling into an effective incoherent hopping process.

The central physical result is that the detector backaction is strongly bias dependent. Both the steady-state current $I(V)$ and the effective dephasing strength $\tilde{\Gamma}^{\mathrm{ss}}(V)$ inherit their structure from the opening and closing of transport channels in the detector. By tuning the bias voltage, one can therefore identify operating regimes where the detector remains sensitive while the induced decoherence is not maximum. This demonstrates that continuous charge sensing does not inevitably lead to maximal decoherence, but rather that an optimal trade-off between measurement contrast and backaction exists.

Conceptual Contributions. Compared to Ref. [10], the present work introduces several conceptual improvements. First, the DQD and the detector are treated within a unified microscopic master-equation framework. The detector current and its fluctuations are not calculated independently of the DQD state. Instead, the detector tunneling processes explicitly depend on the DQD occupation through the interaction terms $U_L\hat{n}_D\hat{n}_L$ and $U_R\hat{n}_D\hat{n}_R$. As a result, transport and decoherence are determined self-consistently from the same steady-state density matrix. Second, the model directly links measurement-induced dephasing to the microscopic jump operators responsible for detector transport. The effective dephasing rate, see in Eq. (3.38), emerges naturally from the population-weighted damping rates, rather than being introduced through an external noise spectrum. Third, the comparison between the full Liouvillian solution and the time-scale separation approximation clarifies the physical regime in which the detector can be viewed as a fast measurement device. The coherent inter-dot tunneling amplitude g is converted into an effective classical transition rate proportional to $|g|^2$, suppressed by detector-induced dephasing. This provides a transparent interpretation of how continuous measurement transforms coherent dynamics into incoherent transport.

Relation to Experimental Observations. The experimental study that motivated this work reports a bias-dependent decoherence rate extracted from microwave spectroscopy mea-

surements. Overall, the extracted decoherence rate increases with detector operating point (e.g., detector current), yet it can also display a plateau-like regime where the decoherence remains essentially unchanged even as both the detector current and the charge sensitivity continue to increase (see Fig. 3(b) in Ref. [10]).

In the present model, the effective dephasing strength follows the same threshold structure as the detector transport channels. Regions of enhanced charge distinguishability coincide with increased backaction, reproducing the qualitative voltage dependence observed experimentally. This indicates that the present model, while self-consistent, still overestimates the effective measurement backaction.

Limitations of the Model. Several simplifying assumptions were made in the present work. First, the detector reservoirs were treated within the standard Born–Markov approximation, assuming energy-independent tunneling densities and neglecting memory effects [15]. Non-Markovian corrections could modify the effective noise spectrum experienced by the DQD and potentially reduce the predicted dephasing strength [16].

Second, the capacitive interaction was modeled as a purely electrostatic density–density coupling. In realistic devices, screening effects and higher-order correlations may partially suppress charge fluctuations, thereby reducing measurement backaction [17].

Finally, the present treatment assumes idealized single-level quantum dots (and effectively neglects spin and excited-state structure). In experimental devices, additional orbital/spin states (and possible valley degeneracies) as well as energy-dependent tunneling amplitudes can reshape the transport characteristics and thereby significantly modify the transport-induced noise spectrum [18].

Weak-measurement regime. A further limitation concerns the measurement strength implied by our approximations. To obtain a time-independent completely positive master equation for the coherent DQD, we employed a secular treatment, which is justified when the conditional detector energies are well separated, $|U_L - U_R| \gg \kappa$, where κ denotes a typical detector relaxation scale. In this regime, detector tunneling events efficiently distinguish the DQD charge configuration and therefore strongly suppress inter-dot coherence. It is natural to ask how this picture changes in a weaker-measurement regime, where $|U_L - U_R|$ becomes comparable to or smaller than the detector relaxation scale.

However, reducing $|U_L - U_R|$ also challenges the assumptions underlying the Born–Markov rates. In particular, the Markovian wide-band description relies on reservoir quantities being slowly varying on the relevant energy-resolution scale, such that $n_F(E + \delta) \simeq n_F(E)$ when δ is within that scale. As a consequence, if $|U_L - U_R| \lesssim \kappa$, the two conditional transport channels become indistinguishable within the present approximation, and the detector current loses its dependence on the DQD state. A consistent theory of weak continuous measurement therefore requires going beyond the strictly secular GKLS limit and/or beyond the energy-independent rate approximation [19], e.g., by employing a partially secular or coarse-grained master equation [20–25] or by explicitly accounting for finite energy resolution of the detector transport.

Outlook. Future extensions of this work could address these limitations in several directions. A natural improvement would be to incorporate non-Markovian effects by deriving a generalized master equation with frequency-dependent rates. This would allow for a more accurate description of the detector charge fluctuation spectrum.

Furthermore, combining the present transport-based description with a microscopic calculation of the detector charge correlation function would enable a direct comparison with experi-

mentally extracted decoherence spectra.

Ultimately, a quantitatively accurate model of continuous charge sensing requires a unified description of transport, measurement backaction, and environmental noise. The present work represents a step toward such a framework by treating detector and DQD dynamics on equal footing.

A Jump operators

This appendix supplements Chapter 2 by providing the intermediate steps that are omitted from the explicit construction of the jump operators via the interaction-picture evolution of dot operators using the BCH expansion.

In the interaction picture with respect to the dot Hamiltonian

$$\hat{H}_{\text{dots}} = \epsilon_D \hat{n}_D + \epsilon_S \hat{n}_S + U \hat{n}_D \hat{n}_S, \tag{A.1}$$

the relevant system coupling operators are $\hat{d}_D$, $\hat{d}_D^\dagger$, $\hat{d}_S$, and $\hat{d}_S^\dagger$ (see main text, Sec. 2.3). We compute their interaction-picture form using the BCH expansion

$$e^X Y e^{-X} = \sum_{n=0}^{\infty} \frac{[X,Y]_n}{n!}, \qquad [X,Y]_0 \equiv Y, \quad [X,Y]_n \equiv [X,[X,Y]_{n-1}], \tag{A.2}$$

with $X = +i\hat{H}_{\text{dots}} t$.

We first note the commutators

$$[\hat{n}_D, \hat{d}_D] = -\hat{d}_D, \qquad [\hat{n}_S, \hat{d}_D] = 0, \qquad [\hat{n}_D \hat{n}_S, \hat{d}_D] = -\hat{n}_S \hat{d}_D, \tag{A.3}$$

and similarly

$$[\hat{n}_S, \hat{d}_S] = -\hat{d}_S, \qquad [\hat{n}_D, \hat{d}_S] = 0, \qquad [\hat{n}_D \hat{n}_S, \hat{d}_S] = -\hat{n}_D \hat{d}_S. \tag{A.4}$$

It is convenient to use the projector decomposition of the opposite-dot occupation,

$$\hat{n}_S^2 = \hat{n}_S, \qquad (1-\hat{n}_S)^2 = (1-\hat{n}_S), \qquad \hat{n}_S(1-\hat{n}_S) = 0, \tag{A.5}$$

and likewise for $\hat{n}_D$.

Using Eqs. (A.2)–(A.3), one finds that $\hat{d}_D$ splits into two components that acquire different phases depending on $\hat{n}_S$:

$$\tilde{d}_D(t) = e^{+i\hat{H}_{\text{dots}}t} \hat{d}_D e^{-i\hat{H}_{\text{dots}}t} = e^{-i\epsilon_D t}\, \hat{d}_D(1-\hat{n}_S) + e^{-i(\epsilon_D+U)t}\, \hat{d}_D \hat{n}_S, \tag{A.6}$$

$$\tilde{d}_D^\dagger(t) = e^{+i\epsilon_D t}\, \hat{d}_D^\dagger(1-\hat{n}_S) + e^{+i(\epsilon_D+U)t}\, \hat{d}_D^\dagger \hat{n}_S. \tag{A.7}$$

Analogously,

$$\tilde{d}_S(t) = e^{-i\epsilon_S t}\, \hat{d}_S(1-\hat{n}_D) + e^{-i(\epsilon_S+U)t}\, \hat{d}_S \hat{n}_D, \tag{A.8}$$

$$\tilde{d}_S^\dagger(t) = e^{+i\epsilon_S t}\, \hat{d}_S^\dagger(1-\hat{n}_D) + e^{+i(\epsilon_S+U)t}\, \hat{d}_S^\dagger \hat{n}_D. \tag{A.9}$$

Equations (A.6)–(A.9) provide the required frequency decomposition into eigenoperators (Bohr-frequency components) used in the main text. They directly imply the jump operators appearing in Eqs. (2.17)-(2.20): for detector reservoirs (D_L, D_R) the channel at $\omega = \epsilon_D$ is associated with $\hat{d}_D(1-\hat{n}_S)$ and $\hat{d}_D^\dagger(1-\hat{n}_S)$, while the channel at $\omega = \epsilon_D + U$ is associated with $\hat{d}_D \hat{n}_S$ and $\hat{d}_D^\dagger \hat{n}_S$ (and analogously for the target reservoir coupled to dot S).

B Calculation of the non-secular part

This appendix has two parts: Sec. B.1 derives the non-secular contributions for the SQD model of Chapter 2, and Sec. B.2 derives the non-secular contributions for the DQD–detector model of Chapter 3.

B.1 SQD model

In Chapter 2, we omitted the intermediate steps leading to the GKLS master equation for the SQD model. For completeness, this appendix presents the corresponding derivation, with emphasis on the contributions arising when the secular approximation is *not* applied.

Secular approximation (GKLS form). Under the secular approximation, the interaction-picture master equation takes the GKLS form

$$\partial_t \tilde{\rho}(t) = \sum_{\alpha,k,j} \gamma_k^{\alpha}(\omega_j)\, \mathcal{D}[\hat{S}^j_{\alpha,k}]\, \tilde{\rho}(t), \tag{B.1}$$

where $\mathcal{D}[\hat{A}]\,\rho \equiv \hat{A}\rho\hat{A}^\dagger - \frac{1}{2}\{\hat{A}^\dagger\hat{A}, \rho\}$. Transforming back to the Schrödinger picture yields

$$\partial_t \hat{\rho}(t) = -i[\hat{H}_S + \hat{H}_{\mathrm{LS}}, \hat{\rho}(t)] + \sum_{\alpha,k,j} \gamma_k^{\alpha}(\omega_j)\, \mathcal{D}[\hat{S}^j_{\alpha,k}]\, \hat{\rho}(t). \tag{B.2}$$

Without secular approximation. If the secular approximation is not invoked, the interaction-picture generator contains additional oscillatory cross terms coupling different Bohr frequencies:

$$\begin{aligned}
\partial_t \tilde{\rho}(t) &= \sum_{\alpha} \sum_{k,k'} \sum_{j,j'} e^{i(\omega_j - \omega_{j'})t}\, \Gamma^{\alpha}_{k,k'}(\omega_j) \Big[\hat{S}^{j'}_{\alpha,k'} \tilde{\rho}(t) \big(\hat{S}^{j}_{\alpha,k}\big)^\dagger - \big(\hat{S}^{j}_{\alpha,k}\big)^\dagger \hat{S}^{j'}_{\alpha,k'} \tilde{\rho}(t) \Big] + \text{H.c.} \\
&= \sum_{\alpha,k,j=j'} \gamma_k^{\alpha}(\omega_j)\, \mathcal{D}[\hat{S}^j_{\alpha,k}]\, \tilde{\rho}(t) + \sum_{\alpha,k} \sum_{j\neq j'} e^{i(\omega_j - \omega_{j'})t}\, \Gamma^{\alpha}_{k}(\omega_j) \Big[\hat{S}^{j'}_{\alpha,k} \tilde{\rho}(t) \big(\hat{S}^{j}_{\alpha,k}\big)^\dagger - \big(\hat{S}^{j}_{\alpha,k}\big)^\dagger \hat{S}^{j'}_{\alpha,k} \tilde{\rho}(t) \Big] + \text{H.c.} \\
&= \gamma_0^{\mathrm{D}_L}(\epsilon_{\mathrm{D}})\, \mathcal{D}[\hat{S}^0_{\mathrm{D}_L,0}]\, \tilde{\rho}(t) + \gamma_1^{\mathrm{D}_L}(\epsilon_{\mathrm{D}})\, \mathcal{D}[\hat{S}^0_{\mathrm{D}_L,1}]\, \tilde{\rho}(t) \\
&+ \gamma_0^{\mathrm{D}_L}(\epsilon_{\mathrm{D}}+U)\, \mathcal{D}[\hat{S}^1_{\mathrm{D}_L,0}]\, \tilde{\rho}(t) + \gamma_1^{\mathrm{D}_L}(\epsilon_{\mathrm{D}}+U)\, \mathcal{D}[\hat{S}^1_{\mathrm{D}_L,1}]\, \tilde{\rho}(t) \\
&\quad + \gamma_0^{\mathrm{D}_R}(\epsilon_{\mathrm{D}})\, \mathcal{D}[\hat{S}^0_{\mathrm{D}_R,0}]\, \tilde{\rho}(t) + \gamma_1^{\mathrm{D}_R}(\epsilon_{\mathrm{D}})\, \mathcal{D}[\hat{S}^0_{\mathrm{D}_R,1}]\, \tilde{\rho}(t) \\
&+ \gamma_0^{\mathrm{D}_R}(\epsilon_{\mathrm{D}}+U)\, \mathcal{D}[\hat{S}^1_{\mathrm{D}_R,0}]\, \tilde{\rho}(t) + \gamma_1^{\mathrm{D}_R}(\epsilon_{\mathrm{D}}+U)\, \mathcal{D}[\hat{S}^1_{\mathrm{D}_R,1}]\, \tilde{\rho}(t) \\
&\quad + \gamma_0^{\mathrm{S}}(\epsilon_{\mathrm{S}})\, \mathcal{D}[\hat{S}^0_{\mathrm{S},0}]\, \tilde{\rho}(t) + \gamma_1^{\mathrm{S}}(\epsilon_{\mathrm{S}})\, \mathcal{D}[\hat{S}^0_{\mathrm{S},1}]\, \tilde{\rho}(t) \\
&+ \gamma_0^{\mathrm{S}}(\epsilon_{\mathrm{S}}+U)\, \mathcal{D}[\hat{S}^1_{\mathrm{S},0}]\, \tilde{\rho}(t) + \gamma_1^{\mathrm{S}}(\epsilon_{\mathrm{S}}+U)\, \mathcal{D}[\hat{S}^1_{\mathrm{S},1}]\, \tilde{\rho}(t) \\
&\quad + \sum_{\alpha,k} \sum_{j\neq j'} e^{i(\omega_j - \omega_{j'})t}\, \Gamma^{\alpha}_{k}(\omega_j) \Big[\hat{S}^{j'}_{\alpha,k} \tilde{\rho}(t) \big(\hat{S}^{j}_{\alpha,k}\big)^\dagger - \big(\hat{S}^{j}_{\alpha,k}\big)^\dagger \hat{S}^{j'}_{\alpha,k} \tilde{\rho}(t) \Big] + \text{H.c.}
\end{aligned}$$

Explicit form of the non-secular contribution. We now evaluate the cross terms ($j \neq j'$),

$$\sum_{\alpha,k}\sum_{j\neq j'} e^{i(\omega_j-\omega_{j'})t}\Gamma^{\alpha}_{k,k'}(\omega_j)\Big[\hat{S}^{j'}_{\alpha,k'}\tilde{\rho}(t)\big(\hat{S}^{j}_{\alpha,k}\big)^\dagger - \big(\hat{S}^{j}_{\alpha,k}\big)^\dagger\hat{S}^{j'}_{\alpha,k'}\tilde{\rho}(t)\Big] + \text{H.c.}$$

for $\alpha = \mathrm{D}_L$, $j,j' = 0,1$, $k = 0$:

$$+ e^{-iUt}\Gamma_0^{\mathrm{D}_L}(\epsilon_D+U)\Big[\hat{d}_{\mathrm{D}}\hat{d}_S^\dagger\hat{d}_{\mathrm{S}}\,\tilde{\rho}(t)\,\hat{d}_{\mathrm{S}}\hat{d}_{\mathrm{S}}^\dagger\hat{d}_{\mathrm{D}}^\dagger - \hat{d}_{\mathrm{S}}\hat{d}_{\mathrm{S}}^\dagger\hat{d}_{\mathrm{D}}^\dagger\hat{d}_{\mathrm{D}}\hat{d}_{\mathrm{S}}^\dagger\hat{d}_{\mathrm{S}}\,\tilde{\rho}(t)\Big]$$

$$+ e^{+iUt}\Gamma_0^{\mathrm{D}_L\,*}(\epsilon_D+U)\Big[\hat{d}_{\mathrm{D}}\hat{d}_{\mathrm{S}}\hat{d}_S^\dagger\,\tilde{\rho}(t)\,\hat{d}_S^\dagger\hat{d}_{\mathrm{S}}\hat{d}_{\mathrm{D}}^\dagger - \tilde{\rho}(t)\,\hat{d}_S^\dagger\hat{d}_{\mathrm{S}}\hat{d}_{\mathrm{D}}^\dagger\hat{d}_{\mathrm{D}}\hat{d}_{\mathrm{S}}\hat{d}_{\mathrm{S}}^\dagger\Big]$$

for $\alpha = \mathrm{D}_L$, $j,j' = 0,1$, $k = 1$:

$$+ e^{-iUt}\Gamma_1^{\mathrm{D}_L}(\epsilon_D+U)\Big[\hat{d}_{\mathrm{D}}^\dagger\hat{d}_S^\dagger\hat{d}_{\mathrm{S}}\,\tilde{\rho}(t)\,\hat{d}_{\mathrm{S}}\hat{d}_{\mathrm{S}}^\dagger\hat{d}_{\mathrm{D}} - \hat{d}_{\mathrm{S}}\hat{d}_{\mathrm{S}}^\dagger\hat{d}_{\mathrm{D}}\hat{d}_{\mathrm{D}}^\dagger\hat{d}_{\mathrm{S}}^\dagger\hat{d}_{\mathrm{S}}\,\tilde{\rho}(t)\Big]$$

$$+ e^{+iUt}\Gamma_1^{\mathrm{D}_L\,*}(\epsilon_D+U)\Big[\hat{d}_{\mathrm{D}}^\dagger\hat{d}_{\mathrm{S}}\hat{d}_S^\dagger\,\tilde{\rho}(t)\,\hat{d}_S^\dagger\hat{d}_{\mathrm{S}}\hat{d}_{\mathrm{D}} - \tilde{\rho}(t)\,\hat{d}_S^\dagger\hat{d}_{\mathrm{S}}\hat{d}_{\mathrm{D}}\hat{d}_{\mathrm{D}}^\dagger\hat{d}_{\mathrm{S}}\hat{d}_{\mathrm{S}}^\dagger\Big]$$

for $\alpha = \mathrm{D}_L$, $j,j' = 1,0$, $k = 0$:

$$+ e^{+iUt}\Gamma_0^{\mathrm{D}_L}(\epsilon_D)\Big[\hat{d}_{\mathrm{D}}\hat{d}_{\mathrm{S}}\hat{d}_S^\dagger\,\tilde{\rho}(t)\,\hat{d}_S^\dagger\hat{d}_{\mathrm{S}}\hat{d}_{\mathrm{D}}^\dagger - \hat{d}_S^\dagger\hat{d}_{\mathrm{S}}\hat{d}_{\mathrm{D}}^\dagger\hat{d}_{\mathrm{D}}\hat{d}_{\mathrm{S}}\hat{d}_{\mathrm{S}}^\dagger\tilde{\rho}(t)\Big]$$

$$+ e^{-iUt}\Gamma_0^{\mathrm{D}_L\,*}(\epsilon_D)\Big[\hat{d}_{\mathrm{D}}\hat{d}_S^\dagger\hat{d}_{\mathrm{S}}\,\tilde{\rho}(t)\,\hat{d}_{\mathrm{S}}\hat{d}_{\mathrm{S}}^\dagger\hat{d}_{\mathrm{D}}^\dagger - \tilde{\rho}(t)\,\hat{d}_{\mathrm{S}}\hat{d}_{\mathrm{S}}^\dagger\hat{d}_{\mathrm{D}}^\dagger\hat{d}_{\mathrm{D}}\hat{d}_{\mathrm{S}}^\dagger\hat{d}_{\mathrm{S}}\Big]$$

for $\alpha = \mathrm{D}_L$, $j,j' = 1,0$, $k = 1$:

$$+ e^{+iUt}\Gamma_1^{\mathrm{D}_L}(\epsilon_D)\Big[\hat{d}_{\mathrm{D}}^\dagger\hat{d}_{\mathrm{S}}\hat{d}_S^\dagger\,\tilde{\rho}(t)\,\hat{d}_S^\dagger\hat{d}_{\mathrm{S}}\hat{d}_{\mathrm{D}} - \hat{d}_S^\dagger\hat{d}_{\mathrm{S}}\hat{d}_{\mathrm{D}}\hat{d}_{\mathrm{D}}^\dagger\hat{d}_{\mathrm{S}}\hat{d}_{\mathrm{S}}^\dagger\tilde{\rho}(t)\Big]$$

$$+ e^{-iUt}\Gamma_1^{\mathrm{D}_L\,*}(\epsilon_D)\Big[\hat{d}_{\mathrm{D}}^\dagger\hat{d}_S^\dagger\hat{d}_{\mathrm{S}}\,\tilde{\rho}(t)\,\hat{d}_{\mathrm{S}}\hat{d}_{\mathrm{S}}^\dagger\hat{d}_{\mathrm{D}} - \tilde{\rho}(t)\,\hat{d}_{\mathrm{S}}\hat{d}_{\mathrm{S}}^\dagger\hat{d}_{\mathrm{D}}\hat{d}_{\mathrm{D}}^\dagger\hat{d}_{\mathrm{S}}\hat{d}_{\mathrm{S}}^\dagger\Big]$$

for $\alpha = \mathrm{S}$, $\ldots$

for $\alpha = \mathrm{D}_R$, $\ldots$

Cancellation of the non-secular terms for the SQD. From the explicit expressions above (illustrated here for the D_L-bath contribution), one encounters terms of the form $\big(\hat{S}^{j}_{\alpha,k}\big)^\dagger\hat{S}^{j'}_{\alpha,k'}\tilde{\rho}(t)$ and its Hermitian conjugate. For the SQD setup considered in Chapter 2, the relevant reduced state remains diagonal in the occupation-number basis (i.e., no coherence is generated between different charge sectors), which can be expressed as

$$[\hat{d}_j^\dagger\hat{d}_j, \hat{\rho}(t)] = 0 \qquad \text{(for the relevant modes } j \text{ in the SQD)}. \tag{B.3}$$

Using fermionic anticommutation relations, the non-secular cross terms proportional to $e^{\pm iUt}$ can then be rearranged into products containing repeated creation operators, and therefore vanish. For instance, for $\alpha = \mathrm{D}_L$, $j,j' = 0,1$, and $k = 0$, we obtain

$$e^{-iUt}\Gamma_0^{\mathrm{D}_L}(\epsilon_D+U)\,\hat{d}_{\mathrm{D}}\,\tilde{\rho}(t)\,\hat{d}_{\mathrm{D}}^\dagger\,\hat{d}_S^\dagger\hat{d}_{\mathrm{S}}\hat{d}_{\mathrm{S}}\hat{d}_{\mathrm{S}}^\dagger \;+\; e^{+iUt}\Gamma_0^{\mathrm{D}_L\,*}(\epsilon_D+U)\,\hat{d}_{\mathrm{D}}\,\tilde{\rho}(t)\,\hat{d}_{\mathrm{D}}^\dagger\,\hat{d}_{\mathrm{S}}\hat{d}_S^\dagger\hat{d}_S^\dagger\hat{d}_{\mathrm{S}} = 0. \tag{B.4}$$

Consequently, the master equation reduces to the secular (GKLS) contribution only:

$$\begin{aligned}\partial_t\tilde{\rho}(t) = {}& \gamma_0^{\mathrm{D}_L}(\epsilon_\mathrm{D})\,\mathcal{D}[\hat{S}^0_{\mathrm{D}_L,0}]\,\tilde{\rho}(t) + \gamma_1^{\mathrm{D}_L}(\epsilon_\mathrm{D})\,\mathcal{D}[\hat{S}^0_{\mathrm{D}_L,1}]\,\tilde{\rho}(t)\\ &+ \gamma_0^{\mathrm{D}_L}(\epsilon_\mathrm{D}+U)\,\mathcal{D}[\hat{S}^1_{\mathrm{D}_L,0}]\,\tilde{\rho}(t) + \gamma_1^{\mathrm{D}_L}(\epsilon_\mathrm{D}+U)\,\mathcal{D}[\hat{S}^1_{\mathrm{D}_L,1}]\,\tilde{\rho}(t)\\ &+ \gamma_0^{\mathrm{D}_R}(\epsilon_\mathrm{D})\,\mathcal{D}[\hat{S}^0_{\mathrm{D}_R,0}]\,\tilde{\rho}(t) + \gamma_1^{\mathrm{D}_R}(\epsilon_\mathrm{D})\,\mathcal{D}[\hat{S}^0_{\mathrm{D}_R,1}]\,\tilde{\rho}(t)\\ &+ \gamma_0^{\mathrm{D}_R}(\epsilon_\mathrm{D}+U)\,\mathcal{D}[\hat{S}^1_{\mathrm{D}_R,0}]\,\tilde{\rho}(t) + \gamma_1^{\mathrm{D}_R}(\epsilon_\mathrm{D}+U)\,\mathcal{D}[\hat{S}^1_{\mathrm{D}_R,1}]\,\tilde{\rho}(t)\\ &+ \gamma_0^{\mathrm{S}}(\epsilon_\mathrm{S})\,\mathcal{D}[\hat{S}^0_{\mathrm{S},0}]\,\tilde{\rho}(t) + \gamma_1^{\mathrm{S}}(\epsilon_\mathrm{S})\,\mathcal{D}[\hat{S}^0_{\mathrm{S},1}]\,\tilde{\rho}(t)\\ &+ \gamma_0^{\mathrm{S}}(\epsilon_\mathrm{S}+U)\,\mathcal{D}[\hat{S}^1_{\mathrm{S},0}]\,\tilde{\rho}(t) + \gamma_1^{\mathrm{S}}(\epsilon_\mathrm{S}+U)\,\mathcal{D}[\hat{S}^1_{\mathrm{S},1}]\,\tilde{\rho}(t).\end{aligned}$$

Finally, transforming back to the Schrödinger picture gives

$$\begin{aligned}\partial_t\hat{\rho}(t) = {}& -i\Big[\epsilon_\mathrm{D}\hat{d}^\dagger_\mathrm{D}\hat{d}_\mathrm{D} + \epsilon_\mathrm{S}\hat{d}^\dagger_\mathrm{S}\hat{d}_\mathrm{S} + U\hat{d}^\dagger_\mathrm{D}\hat{d}_\mathrm{D}\,\hat{d}^\dagger_\mathrm{S}\hat{d}_\mathrm{S} + \hat{H}_\mathrm{LS}, \hat{\rho}(t)\Big]\\ &+ \gamma_0^{\mathrm{D}_L}(\epsilon_\mathrm{D})\mathcal{D}[\hat{S}^0_{\mathrm{D}_L,0}]\,\hat{\rho}(t) + \gamma_1^{\mathrm{D}_L}(\epsilon_\mathrm{D})\mathcal{D}[\hat{S}^0_{\mathrm{D}_L,1}]\,\hat{\rho}(t)\\ &+ \gamma_0^{\mathrm{D}_L}(\epsilon_\mathrm{D}+U)\mathcal{D}[\hat{S}^1_{\mathrm{D}_L,0}]\,\hat{\rho}(t) + \gamma_1^{\mathrm{D}_L}(\epsilon_\mathrm{D}+U)\mathcal{D}[\hat{S}^1_{\mathrm{D}_L,1}]\,\hat{\rho}(t)\\ &+ \gamma_0^{\mathrm{D}_R}(\epsilon_\mathrm{D})\mathcal{D}[\hat{S}^0_{\mathrm{D}_R,0}]\,\hat{\rho}(t) + \gamma_1^{\mathrm{D}_R}(\epsilon_\mathrm{D})\mathcal{D}[\hat{S}^0_{\mathrm{D}_R,1}]\,\hat{\rho}(t)\\ &+ \gamma_0^{\mathrm{D}_R}(\epsilon_\mathrm{D}+U)\mathcal{D}[\hat{S}^1_{\mathrm{D}_R,0}]\,\hat{\rho}(t) + \gamma_1^{\mathrm{D}_R}(\epsilon_\mathrm{D}+U)\mathcal{D}[\hat{S}^1_{\mathrm{D}_R,1}]\,\hat{\rho}(t)\\ &+ \gamma_0^{\mathrm{S}}(\epsilon_\mathrm{S})\mathcal{D}[\hat{S}^0_{\mathrm{S},0}]\,\hat{\rho}(t) + \gamma_1^{\mathrm{S}}(\epsilon_\mathrm{S})\mathcal{D}[\hat{S}^0_{\mathrm{S},1}]\,\hat{\rho}(t)\\ &+ \gamma_0^{\mathrm{S}}(\epsilon_\mathrm{S}+U)\mathcal{D}[\hat{S}^1_{\mathrm{S},0}]\,\hat{\rho}(t) + \gamma_1^{\mathrm{S}}(\epsilon_\mathrm{S}+U)\mathcal{D}[\hat{S}^1_{\mathrm{S},1}]\,\hat{\rho}(t).\end{aligned}$$

B.2 DQD model

The derivation above illustrates how the GKLS master equation is obtained for the SQD model. We now outline the corresponding construction for the DQD case.

Similarly to the SQD case, the coupling Hamiltonian for bath α is written as

$$\hat{V}_\alpha = \hat{S}_{\alpha,0}\hat{B}_{\alpha,0} + \hat{S}_{\alpha,1}\hat{B}_{\alpha,1}. \tag{B.5}$$

The corresponding jump operators are obtained from the interaction-picture system operators using the Baker–Campbell–Hausdorff (BCH) expansion.

$$\begin{aligned}\tilde{S}_{L,0}(t) = {}& e^{-i\epsilon_D t}\,\hat{d}_D\,\hat{d}_L\hat{d}^\dagger_L\,\hat{d}_R\hat{d}^\dagger_R + e^{-i(\epsilon_D+U_L)t}\,\hat{d}_D\,\hat{d}^\dagger_L\hat{d}_L\,\hat{d}_R\hat{d}^\dagger_R\\ &+ e^{-i(\epsilon_D+U_R)t}\,\hat{d}_D\,\hat{d}_L\hat{d}^\dagger_L\,\hat{d}^\dagger_R\hat{d}_R + e^{-i(\epsilon_D+U_L+U_R)t}\,\hat{d}_D\,\hat{d}^\dagger_L\hat{d}_L\,\hat{d}^\dagger_R\hat{d}_R, \qquad \text{(B.6)}\\ \tilde{S}_{L,1}(t) = {}& e^{+i\epsilon_D t}\,\hat{d}^\dagger_D\,\hat{d}_L\hat{d}^\dagger_L\,\hat{d}_R\hat{d}^\dagger_R + e^{+i(\epsilon_D+U_L)t}\,\hat{d}^\dagger_D\,\hat{d}^\dagger_L\hat{d}_L\,\hat{d}_R\hat{d}^\dagger_R\\ &+ e^{+i(\epsilon_D+U_R)t}\,\hat{d}^\dagger_D\,\hat{d}_L\hat{d}^\dagger_L\,\hat{d}^\dagger_R\hat{d}_R + e^{+i(\epsilon_D+U_L+U_R)t}\,\hat{d}^\dagger_D\,\hat{d}^\dagger_L\hat{d}_L\,\hat{d}^\dagger_R\hat{d}_R. \qquad \text{(B.7)}\end{aligned}$$

We then decompose $\tilde{S}_{\alpha,k}(t)$ into Fourier components,

$$\tilde{S}_{\alpha,k}(t) = \sum_j e^{-i\omega_j t}\,\hat{S}^j_{\alpha,k}, \tag{B.8}$$

which yields the four jump operators (shown here for $k = 0$):

$$\hat{S}^1_{\alpha,0} = \hat{d}_D\, \hat{d}_L \hat{d}_L^\dagger\, \hat{d}_R \hat{d}_R^\dagger, \tag{B.9}$$

$$\hat{S}^2_{\alpha,0} = \hat{d}_D\, \hat{d}_L^\dagger \hat{d}_L\, \hat{d}_R \hat{d}_R^\dagger, \tag{B.10}$$

$$\hat{S}^3_{\alpha,0} = \hat{d}_D\, \hat{d}_L \hat{d}_L^\dagger\, \hat{d}_R^\dagger \hat{d}_R, \tag{B.11}$$

$$\hat{S}^4_{\alpha,0} = \hat{d}_D\, \hat{d}_L^\dagger \hat{d}_L\, \hat{d}_R^\dagger \hat{d}_R. \tag{B.12}$$

These four operators correspond to detector tunneling events conditioned on the occupation configuration of the DQD:

- $\hat{S}^1_{\alpha,0} = \hat{d}_D \hat{d}_L \hat{d}_L^\dagger \hat{d}_R \hat{d}_R^\dagger$ describes the annihilation of a detector electron when the DQD is empty ($n_L = n_R = 0$), with energy ϵ_D.
- $\hat{S}^2_{\alpha,0} = \hat{d}_D \hat{d}_L^\dagger \hat{d}_L \hat{d}_R \hat{d}_R^\dagger$ corresponds to $n_L = 1, n_R = 0$, with energy $\epsilon_D + U_L$.
- $\hat{S}^3_{\alpha,0} = \hat{d}_D \hat{d}_L \hat{d}_L^\dagger \hat{d}_R^\dagger \hat{d}_R$ corresponds to $n_L = 0, n_R = 1$, with energy $\epsilon_D + U_R$.
- $\hat{S}^4_{\alpha,0} = \hat{d}_D \hat{d}_L^\dagger \hat{d}_L \hat{d}_R^\dagger \hat{d}_R$ corresponds to $n_L = n_R = 1$, with energy $\epsilon_D + U_L + U_R$.

In summary, the four jump operators implement detector tunneling processes conditioned on the four charge configurations of the DQD (empty, left occupied, right occupied, and doubly occupied). Each configuration produces a different electrostatic shift of the detector level via capacitive coupling.

Master equation and separation into secular/non-secular parts. The interaction-picture master equation reads

$$\begin{aligned}
\partial_t \tilde{\rho}_S(t) &= \sum_{\alpha,k,k'} \sum_{j,j'} e^{i(\omega_j - \omega_{j'})t} \Gamma^\alpha_{k,k'}(\omega_j) \Big[\hat{S}^{j'}_{\alpha,k'} \tilde{\rho}_S(t) \big(\hat{S}^j_{\alpha,k}\big)^\dagger - \big(\hat{S}^j_{\alpha,k}\big)^\dagger \hat{S}^{j'}_{\alpha,k'} \tilde{\rho}_S(t) \Big] + \text{H.c.} \\
&= \sum_{\alpha,k,j=j'} \gamma^\alpha_k(\omega_j) \mathcal{D}[\hat{S}^j_{\alpha,k}] \tilde{\rho}_S(t) + \sum_{\alpha,k} \sum_{j \neq j'} e^{i(\omega_j - \omega_{j'})t} \Gamma^\alpha_k(\omega_j) \Big[\hat{S}^{j'}_{\alpha,k} \tilde{\rho}_S(t) \big(\hat{S}^j_{\alpha,k}\big)^\dagger - \big(\hat{S}^j_{\alpha,k}\big)^\dagger \hat{S}^{j'}_{\alpha,k} \tilde{\rho}_S(t) \Big] + \text{H.c.} \\
&= \gamma^\alpha_0(\epsilon_D) \mathcal{D}[\hat{S}^1_{\alpha,0}] \tilde{\rho}_S(t) + \gamma^\alpha_1(\epsilon_D) \mathcal{D}[\hat{S}^1_{\alpha,1}] \tilde{\rho}_S(t) \\
&\quad + \gamma^\alpha_0(\epsilon_D + U_L) \mathcal{D}[\hat{S}^2_{\alpha,0}] \tilde{\rho}_S(t) + \gamma^\alpha_1(\epsilon_D + U_L) \mathcal{D}[\hat{S}^2_{\alpha,1}] \tilde{\rho}_S(t) \\
&\quad + \gamma^\alpha_0(\epsilon_D + U_R) \mathcal{D}[\hat{S}^3_{\alpha,0}] \tilde{\rho}_S(t) + \gamma^\alpha_1(\epsilon_D + U_R) \mathcal{D}[\hat{S}^3_{\alpha,1}] \tilde{\rho}_S(t) \\
&\quad + \gamma^\alpha_0(\epsilon_D + U_L + U_R) \mathcal{D}[\hat{S}^4_{\alpha,0}] \tilde{\rho}_S(t) + \gamma^\alpha_1(\epsilon_D + U_L + U_R) \mathcal{D}[\hat{S}^4_{\alpha,1}] \tilde{\rho}_S(t) \\
&\quad + \sum_{\alpha,k} \sum_{j \neq j'} e^{i(\omega_j - \omega_{j'})t} \Gamma^\alpha_k(\omega_j) \Big[\hat{S}^{j'}_{\alpha,k} \tilde{\rho}_S(t) \big(\hat{S}^j_{\alpha,k}\big)^\dagger - \big(\hat{S}^j_{\alpha,k}\big)^\dagger \hat{S}^{j'}_{\alpha,k} \tilde{\rho}_S(t) \Big] + \text{H.c.}
\end{aligned}$$

Non-secular contribution. As an example, for the pair $(j, j') = (2, 3)$ and $k = 0$, one obtains an oscillatory term at frequency $U_L - U_R$,

$$\sum_{\alpha,k} \sum_{j \neq j'} e^{i(\omega_j - \omega_{j'})t} \Gamma^\alpha_{k,k'}(\omega_j) \left[\hat{S}^{j'}_{\alpha,k'} \tilde{\rho}_S(t) \left(\hat{S}^j_{\alpha,k}\right)^\dagger - \left(\hat{S}^j_{\alpha,k}\right)^\dagger \hat{S}^{j'}_{\alpha,k'} \tilde{\rho}_S(t) \right] + \text{H.c.} =$$

for $j, j' = 2, 3 \quad k = 0$:

$$+ e^{-i(U_L - U_R)t} \Gamma^\alpha_0(\epsilon_D + U_L) [d_D[(1 - n_L) n_R] \tilde{\rho}_S(t) [n_L(1 - n_R)] d_D^\dagger - [n_L(1 - n_R)] d_D^\dagger d_D [(1 - n_L) n_R] \tilde{\rho}_S(t)]$$

for $\alpha = D_L \quad j, j' = 0, 1 \quad k = 0:$

$$e^{-iUt}\Gamma_0^{\mathrm{D}_L}(\epsilon_D + U_L) d_{\mathrm{D}} d_S^\dagger d_{\mathrm{S}} \tilde{\rho}_S(t) d_{\mathrm{S}} d_{\mathrm{S}}^\dagger d_{\mathrm{D}}^\dagger + e^{+iUt}\Gamma_0^{\mathrm{D}_L\,*}(\epsilon_D + U_L) d_{\mathrm{D}} d_{\mathrm{S}} d_S^\dagger \tilde{\rho}_S(t) d_S^\dagger d_{\mathrm{S}} d_{\mathrm{D}}^\dagger$$

for $\alpha = D_L \quad j, j' = 0, 1 \quad k = 1:$

$$e^{-iUt}\Gamma_1^{\mathrm{D}_L}(\epsilon_D + U_L) [d_{\mathrm{D}}^\dagger d_S^\dagger d_{\mathrm{S}} \tilde{\rho}_S(t) d_{\mathrm{S}} d_{\mathrm{S}}^\dagger d_{\mathrm{D}} + e^{+iUt}\Gamma_1^{\mathrm{D}_L\,*}(\epsilon_D + U_L) d_{\mathrm{D}}^\dagger d_{\mathrm{S}} d_S^\dagger \tilde{\rho}_S(t) d_S^\dagger d_{\mathrm{S}} d_{\mathrm{D}}$$

for $\alpha = D_L \quad j, j' = 1, 0 \quad k = 0:$

$$e^{+iUt}\Gamma_1^{\mathrm{D}_L}(\epsilon_D) d_{\mathrm{D}} d_{\mathrm{S}} d_D^\dagger \tilde{\rho}_S(t) d_D^\dagger d_{\mathrm{S}} d_{\mathrm{D}}^\dagger + e^{-iUt}\Gamma_1^{\mathrm{D}_L\,*}(\epsilon_D) d_{\mathrm{D}} d_S^\dagger d_{\mathrm{S}} \tilde{\rho}_S(t) d_{\mathrm{S}} d_{\mathrm{S}}^\dagger d_{\mathrm{D}}^\dagger$$

for $\alpha = D_L \quad j, j' = 1, 0 \quad k = 1:$

$$e^{+iUt}\Gamma_1^{\mathrm{D}_L}(\epsilon_D) d_{\mathrm{D}}^\dagger d_{\mathrm{S}} d_S^\dagger \tilde{\rho}_S(t) d_S^\dagger d_{\mathrm{S}} d_{\mathrm{D}} + e^{-iUt}\Gamma_1^{\mathrm{D}_L\,*}(\epsilon_D) d_{\mathrm{D}}^\dagger d_S^\dagger d_{\mathrm{S}} \tilde{\rho}_S(t) d_{\mathrm{S}} d_{\mathrm{S}}^\dagger d_{\mathrm{D}}$$

Substituting Eq. (2.24) into the master equation, we obtain

$$\begin{aligned}
\partial_t \hat{\rho}_S(t) &= -i[\hat{H}_S + \hat{H}_{\mathrm{LS}}, \hat{\rho}_S(t)] \\
&\quad + \Big[\kappa_L \big[1 - n_F^L(\epsilon_D + U_L)\big] \mathcal{D}[\hat{d}_D \hat{n}_L] \hat{\rho}_S(t) + \kappa_L n_F^L(\epsilon_D + U_L) \mathcal{D}[\hat{d}_D^\dagger \hat{n}_L] \hat{\rho}_S(t) \\
&\quad\quad + \kappa_L \big[1 - n_F^L(\epsilon_D + U_R)\big] \mathcal{D}[\hat{d}_D \hat{n}_R] \hat{\rho}_S(t) + \kappa_L n_F^L(\epsilon_D + U_R) \mathcal{D}[\hat{d}_D^\dagger \hat{n}_R] \hat{\rho}_S(t)\Big] \\
&\quad + \Big[\kappa_R \big[1 - n_F^R(\epsilon_D + U_R)\big] \mathcal{D}[\hat{d}_D \hat{n}_R] \hat{\rho}_S(t) + \kappa_R n_F^R(\epsilon_D + U_R) \mathcal{D}[\hat{d}_D^\dagger \hat{n}_R] \hat{\rho}_S(t) \\
&\quad\quad + \kappa_R \big[1 - n_F^R(\epsilon_D + U_L)\big] \mathcal{D}[\hat{d}_D \hat{n}_L] \hat{\rho}_S(t) + \kappa_R n_F^R(\epsilon_D + U_L) \mathcal{D}[\hat{d}_D^\dagger \hat{n}_L] \hat{\rho}_S(t)\Big] \qquad \text{(B.13)} \\
&= -i[\hat{H}_S + \hat{H}_{\mathrm{LS}}, \hat{\rho}_S(t)] + \sum_{\alpha \in \{L,R\}} \sum_{\beta \in \{L,R\}} \Big(\Gamma^0_{\alpha,\beta}\, \mathcal{D}[\hat{d}_D \hat{n}_\beta] + \Gamma^1_{\alpha,\beta}\, \mathcal{D}[\hat{d}_D^\dagger \hat{n}_\beta]\Big) \hat{\rho}_S(t). \qquad \text{(B.14)}
\end{aligned}$$

Here,

$$\Gamma^0_{\alpha,\beta} = \kappa_\alpha \big[1 - n_F^\alpha(\epsilon_D + U_\beta)\big], \qquad \Gamma^1_{\alpha,\beta} = \kappa_\alpha\, n_F^\alpha(\epsilon_D + U_\beta). \qquad \text{(B.15)}$$

References

[1] M. Kjaergaard et al. "Superconducting qubits: Current state of play". In: *Annual Review of Condensed Matter Physics* 11 (2020), pp. 369–395. DOI: 10.1146/annurev-conmatphys-031119-050605. arXiv: 1905.13641 [cond-mat.mes-hall].

[2] G. Burkard et al. "Semiconductor spin qubits". In: *Reviews of Modern Physics* 95 (2023), p. 025003. DOI: 10.1103/RevModPhys.95.025003.

[3] Daniel Loss and David P. DiVincenzo. "Quantum computation with quantum dots". In: *Phys. Rev. A* 57 (1 Jan. 1998), pp. 120–126. DOI: 10.1103/PhysRevA.57.120. URL: https://link.aps.org/doi/10.1103/PhysRevA.57.120.

[4] A. Chatterjee et al. "Semiconductor qubits in practice". In: *Nature Reviews Physics* 3 (2021), pp. 157–177. DOI: 10.1038/s42254-021-00283-9.

[5] Yasunobu Nakamura, Yuri A. Pashkin, and Jaw-Shen Tsai. "Coherent control of macroscopic quantum states in a single-Cooper-pair box". In: *Nature* 398.6730 (Apr. 1999), pp. 786–788. DOI: 10.1038/19718. URL: https://doi.org/10.1038/19718.

[6] J. M. Elzerman et al. "Few-electron quantum dot circuit with integrated charge read out". In: *Physical Review B* 67 (2003), 161308(R). DOI: 10.1103/PhysRevB.67.161308. URL: https://link.aps.org/doi/10.1103/PhysRevB.67.161308.

[7] B. Küng et al. "Time-resolved charge detection with cross-correlation techniques". In: *Physical Review B* 79 (2009), p. 035314. DOI: 10.1103/PhysRevB.79.035314. URL: https://link.aps.org/doi/10.1103/PhysRevB.79.035314.

[8] W. Lu et al. "Real-time detection of electron tunnelling in a quantum dot". In: *Nature* 423 (2003), pp. 422–425. DOI: 10.1038/nature01686. URL: https://www.nature.com/articles/nature01686.

[9] T. Fujisawa et al. "Electron counting of single-electron tunneling current". In: *Applied Physics Letters* 84 (2004), pp. 2343–2345. DOI: 10.1063/1.1697627. URL: https://doi.org/10.1063/1.1697627.

[10] Subhomoy Haldar et al. "Coherence of an Electronic Two-Level System under Continuous Charge Sensing by a Quantum Dot Detector". In: *Phys. Rev. Lett.* 134 (2 Jan. 2025), p. 023601. DOI: 10.1103/PhysRevLett.134.023601. URL: https://link.aps.org/doi/10.1103/PhysRevLett.134.023601.

[11] Heinz-Peter Breuer and Francesco Petruccione. *The Theory of Open Quantum Systems*. Oxford: Oxford University Press, 2007. DOI: 10.1093/acprof:oso/9780199213900.001.0001. URL: https://doi.org/10.1093/acprof:oso/9780199213900.001.0001 (visited on 02/24/2026).

[12] Patrick P. Potts. *Quantum Thermodynamics*. June 2024. DOI: 10.48550/arXiv.2406.19206. arXiv: 2406.19206. URL: https://arxiv.org/abs/2406.19206.

[13] Vittorio Gorini, Andrzej Kossakowski, and E. C. G. Sudarshan. "Completely positive dynamical semigroups of N-level systems". In: *Journal of Mathematical Physics* 17.5 (1976), pp. 821–825. DOI: 10.1063/1.522979.

[14] Göran Lindblad. "On the generators of quantum dynamical semigroups". In: *Communications in Mathematical Physics* 48.2 (1976), pp. 119–130. DOI: 10.1007/BF01608499.

[15] S. A. Gurvitz. "Measurements with a noninvasive detector and dephasing mechanism". In: *Phys. Rev. B* 56 (23 Dec. 1997), pp. 15215–15223. DOI: 10.1103/PhysRevB.56.15215. URL: https://link.aps.org/doi/10.1103/PhysRevB.56.15215.

[16] Ming-Tsung Lee and Wei-Min Zhang. "Non-Markovian suppression of charge qubit decoherence in the quantum point contact measurement". In: *The Journal of Chemical Physics* 129.22 (Dec. 2008), p. 224106. DOI: 10.1063/1.3036114. URL: https://doi.org/10.1063/1.3036114.

[17] Markus Büttiker and Andrew M. Martin. "Charge relaxation and dephasing in Coulomb-coupled conductors". In: *Phys. Rev. B* 61 (4 Jan. 2000), pp. 2737–2741. DOI: 10.1103/PhysRevB.61.2737. URL: https://link.aps.org/doi/10.1103/PhysRevB.61.2737.

[18] W. G. van der Wiel et al. "Electron transport through double quantum dots". In: *Rev. Mod. Phys.* 75 (1 Dec. 2002), pp. 1–22. DOI: 10.1103/RevModPhys.75.1. URL: https://link.aps.org/doi/10.1103/RevModPhys.75.1.

[19] Patrick P. Potts, Alex Arash Sand Kalaee, and Andreas Wacker. "A thermodynamically consistent Markovian master equation beyond the secular approximation". In: *New Journal of Physics* 23 (2021), p. 123013. DOI: 10.1088/1367-2630/ac3b2f.

[20] Stella Seah, Stefan Nimmrichter, and Valerio Scarani. "Refrigeration beyond weak internal coupling". In: *Physical Review E* 98 (2018), p. 012131. DOI: 10.1103/PhysRevE.98.012131.

[21] Gernot Schaller and Tobias Brandes. "Preservation of positivity by dynamical coarse graining". In: *Physical Review A* 78 (2008), p. 022106. DOI: 10.1103/PhysRevA.78.022106.

[22] Christian Majenz et al. "Coarse graining can beat the rotating-wave approximation in quantum Markovian master equations". In: *Physical Review A* 88 (2013), p. 012103. DOI: 10.1103/PhysRevA.88.012103.

[23] J. D. Cresser and C. Facer. *Coarse-graining in the derivation of Markovian master equations and its significance in quantum thermodynamics*. 2017. DOI: 10.48550/arXiv.1710.09939. arXiv: 1710.09939 [quant-ph].

[24] Donato Farina and Vittorio Giovannetti. "Open-quantum-system dynamics: recovering positivity of the Redfield equation via the partial secular approximation". In: *Physical Review A* 100 (2019), p. 012107. DOI: 10.1103/PhysRevA.100.012107.

[25] Evgeny Mozgunov and Daniel Lidar. "Completely positive master equation for arbitrary driving and small level spacing". In: *Quantum* 4 (2020), p. 227. DOI: 10.22331/q-2020-02-06-227.

University of Basel

Faculty of Science

Declaration on Scientific Integrity

(including a Declaration on Plagiarism and Fraud)
Translation from German original

Title of Thesis: Markovian Master Equation for Continuous Charge Detection

Name of Assessor: Prof. Dr. Patrick P. Potts

First Name, Surname: Qiuhan Wang

Matriculation No.: 23-065-139

I attest with my signature that I have written this work independently and without outside help. I also attest that the information concerning the sources used in this work is true and complete in every respect. All sources that have been quoted or paraphrased have been marked accordingly. I have mentioned all source materials used and have cited these in accordance with recognized scientific rules.

Additionally, I affirm that any text passages written with the help of AI-supported technology are marked as such, including a reference to the AI-supported program used.
This paper may be checked for plagiarism and use of AI-supported technology using the appropriate software. I understand that unethical conduct may lead to a grade of 1 or "fail" or expulsion from the study program.

Place, Date: Basel, 1/3/2026 Signature of the Student: Qiuhan Wang

Will this work, or parts of it, be published?.

☐ No
☒ Yes. With my signature I confirm that I agree to a publication of the work (print/digital) in the library, on the research database of the University of Basel and/or on the document server of the department. Likewise, I agree to the bibliographic reference in the catalog SLSP (Swiss Library Service Platform). (cross out as applicable)

Publication as of: 1/3/2026

Place, Date: Basel, 1/3/2026 Signature of the Student: Qiuhan Wang

Place, Date: _____ Signature of the Assessor: _____

.